POLITECNICO DI TORINO

DIPARTIMENTO DI ELETTRONICA E TELECOMUNICAZIONI (DET)

Master's Degree in Electronic Engineering

Master's Degree Thesis

One-photon calcium imaging in C. elegans with a novel acousto-optic technique

Supervisor
Prof. Danilo Demarchi

Candidate
Daniele Busacchio

October, 2018

Abstract

One-photon (1P) imaging and optical stimulation are two powerful tools widely used to assess and monitor the behaviour of individual and multiple neurons in *in-vivo* and *ex-vivo* experiments. However, standard 1P microscopes are limited by diffraction and scattering, which reduce the maximum optical depth achievable to few hundreds of micrometres deep into brain tissues. To overcome this issue, implantable waveguides and probes (i.e. optical fibres) are commonly used, but they are highly-invasive and may lead to damage the surrounding tissue.
In this work, it has been developed a customized 1P setup fully compatible with an innovative acousto-optic technology based on an cylindrical piezoelectric transducer, which allows to sculpt a non-invasive virtual waveguide within the tissue, by locally changing its refractive index. Indeed, this technology is capable to deliver and confine light in tissue phantoms with optical thickness (OT) up to 18.8 Mean-Free-Path (MFP) and to perform imaging in turbid media (OT up to 5.9 MFP).
Furthermore, not all laboratories are allowed to use model animals such as monkeys or mice in their experiments, because adequate facilities and surgical skills are needed. Moreover, *ex-vivo* experiments are complex and time-limited, since specimens need special treatments in order to be kept alive and, anyway, after a couple of hours they are no longer able to be used, as clinically dead. For this purpose, here is presented a new concept, cost-effective brain tissue phantom, which exploits living transgenic *Caenorhabditis elegans* (C. elegans) to replicate the structure of a living brain tissue. This can be easily used as proof of concept demonstration of new applications in experiments like electrophysiology, or optogenetics.
The setup has been tested by carrying out experiments on fixed mouse brain slices with green fluorescent protein (GFP) and on living GCaMP6s *C. elegans*.

Keywords: One-photon microscopy, calcium imaging, acousto-optic waveguide, light penetration depth in tissue, GCaMP6s Caenorhabditis elegans.

Contents

List of Figures

List of Acronyms

1P	One-Photon
OT	Optical Thickness
MFP	Mean-Free-Path
GFP	Green Fluorescent Protein
MEA	Multi-Electrode Array
GECI	Genetically Encoded Calcium Indicator
VGIC	Voltage-Gated Ion Channels
2P	Two-Photon
LED	Light Emitting Diode
GRIN	Graded Index
UV	Ultraviolet
IR	Infrared
NA	Numerical Aperture
WD	Working Distance
VLWD	Very Long Working Distance
FOV	Field Of View
CCD	Charge-Coupled Device
CMOS	Complementary Metal-Oxide Semiconductor
ADC	Analog-to-Digital Converter
FPS	Frame Per Second
SNR	Signal-to-Noise Ratio
DI	De-Ionized
NGM	Nematode Growth Medium

Introduction

Neuronal networks are responsible for information processing, but the mechanisms that regulate their functioning are not completely clear, yet; understanding how they work would lead to understand how to manipulate higher brain functions.

Over the years, many different techniques and tools have been developed in order to assess and monitor the activity of individual and multiple neurons. Indeed, nowadays neuroscientists are able to perform experiments as electrophysiology that allow them to characterise electrical properties of neuron cells, by recording and measuring their electrical activity (e.g., action potentials [1]). According to different applications, it is possible to choose among a variety of recording and stimulation techniques, from patch-clamping on a single cell, to Multi-Electrode Arrays (MEAs) [2][3][4][5]. However, since a direct physical contact between cells and electrodes is needed, these techniques are highly-invasive, causing a reduction of the cell lifespan and, in the worst cases, a damage of the surrounding tissue. For this reason, many researchers are enhancing their effort in optimizing these techniques, e.g., by employing smaller and flexible probes.

Another powerful tool on which neuroscientists can rely is called optogenetics [6][7]. It has been developed over the recent years and it allows researchers to investigate optically neuronal activities in living and even freely-moving animals, like rodents (i.e. rats and mice [8]), or invertebrate (e.g., flies and worms [9][10]). In particular, this method is very helpful to identify which are the neurons, hence the circuit mechanisms, involved in diseases and pathological status [11][12][13]. Such a technique could not have been developed without the so-called Genetically Encoded Calcium Indicators, or GECIs, which paved the way to fluorometric calcium (Ca^{2+}) imaging and, therefore, to optogenetics [14][15][16][17][18]. Nevertheless, since this method exploits the light as a mean to stimulate and assess neurons activities, its effectiveness is highly limited by all the optical properties of the brain tissue, which give origin to optical phenomena (e.g., diffraction and scattering).

All the above mentioned experiments are carried out by employing the so-called animal models. Such a name is due to the fact that they are animals with a wealth of biological data and they can be used to research human diseases, as they meet a determined taxonomic equivalence to humans [19][20]. Researchers decide which one of them better suits with the constraints and the goal of their study. In fact, it is possible to choose animals according to several traits e.g., size, genetics, generation time and manipulation. However, laboratories can be limited by special requirements needed for dealing with living animals like mice, or monkeys. In those cases, animal facilities and surgical skills are mandatory and severe protocols must be followed. This may prevent laboratories

from performing *in-vivo* experiments. One solution to this issue could be to switch from *in-vivo* to *ex-vivo* tests [21]. The main drawback of this kind of experiments is that the brain tissue has to be kept alive for all the time, as otherwise no neurons activity could be neither stimulated, nor recorded. Therefore, specimens are placed inside a so-called perfusion chamber, in which a brain-like environment is replicated, so that the samples can receive the required treatment (e.g., drugs) to maintain them as they were alive [22]. Nevertheless, it is impossible to replicate exactly a brain environment, therefore, the brain tissue inside the perfusion chamber starts gradually to deteriorate, until it turns to be clinically dead after few hours.

This thesis wants to provide a suitable and valid alternative to standard one-photon microscopes, in order to enhance their optical performances either in imaging, or in stimulation. Indeed, by employing an innovative acousto-optic technology, based on a cylindrical piezoelectric transducer, it is possible to reduce the above mentioned optical phenomena (i.e. diffraction and scattering of light inside tissues) that highly affect the optical depth of 1P microscopes. Lastly, a customizable, cost-effective and easy-to-replicate brain tissue phantom, based on living GCaMP6s *C. elegans* is presented. This new model is a valid solution to overcome the possible limitations related to the strict requirements for *in-vivo* experiments on animal models like rodents, or monkeys, as well as for *ex-vivo* tests. In this way, researchers can perform their experiments in transgenic living samples that replicate some features of a brain tissue.
Therefore, the outline of this thesis is the following:

- Chapter 1: overview about calcium imaging and 1P microscopy;
- Chapter 2: description of the working principle of the acousto-optic technology with two example of applications (i.e. *virtual optical waveguide* and *virtual relay lens*);
- Chapter 3: characterisation of the developed customized 1P setup;
- Chapter 4: description of the living brain tissue phantom;
- Chapter 5: results and discussion.

Chapter 1

Calcium Imaging

In this chapter, it is explained the operating principle (and its most important features) that is at the base of the calcium imaging theory. Furthermore, a brief overview and comparison between two possible calcium imaging-based microscopy is provided.

Fluorometric calcium (Ca^{2+}) imaging is one of the many different techniques that have been developed over the recent years to evaluate the function of neuronal networks. It has permitted studies of calcium signalling in a large variety of cells, as well as neuronal activity in many neurons and other cells within nervous systems (e.g., glial cells). Furthermore, calcium imaging not only allows real-time analyses of individual cells, but it also enables simultaneous recordings from many single cells [23].

It exploits the presence of voltage-gated ion channels (VGIC) in living cells and the correspondent ions flowing which pass through them (Figure 1.1). There are four different VGIC in each cell, according to the specific related ion: Na^+, K^+, Ca^{2+} and Cl^-. These channels are sensitive to voltage variations across the membrane. Usually, the inner side of the membrane is at a negative voltage; when it becomes less negative, the pore starts to open, allowing selected ions to cross the channel.

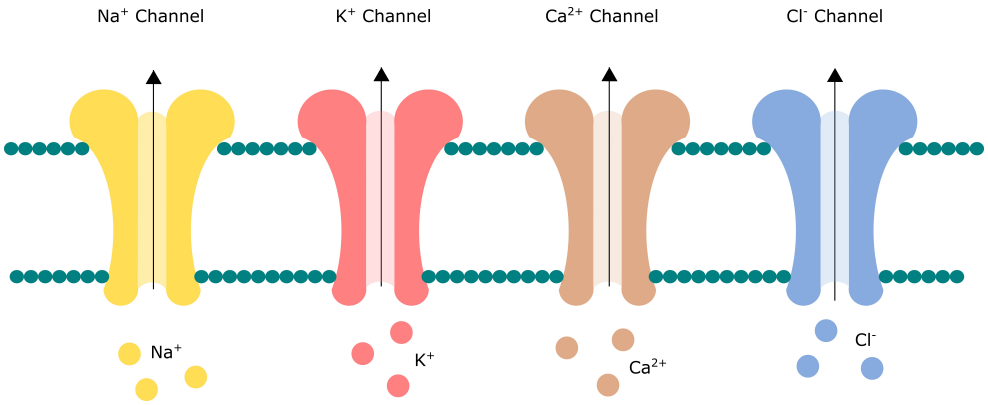

Figure 1.1: Drawing of the four VGIC across the cell membrane. When the inner voltage membrane increases, the channels will let the ions flowing through the membrane.

As the name itself suggests, this technique takes into account calcium channels and, therefore, calcium signals. The reason is that such signals are essential for either basic forms of neuronal communication, or complex processes, therefore there is a high calcium ions exchange during neuronal activities.

In order to assess calcium signals and then neuronal activities, Ca^{2+} imaging makes use of the so-called calcium indicators, or fluorophores, which are fluorescent proteins that change their fluorescence properties when they are bonded to calcium ions. Thanks to this feature, it is possible to optically probe intracellular calcium in living animals.

1.1 Fluorescence

Fluorescence is one of the many processes which belong to the luminescence family of phenomena in which chemical, physical, or mechanical events allow molecules to emit light, as a result of an electronic transition from an excited singlet state to its singlet ground state. In this section [24], only physical mechanisms are taken into account, since strictly related to calcium imaging.

To fully understand how fluorescence works, it is necessary to have clearly understood what the interaction between photons and electrons involves. In Figure 1.2 it is shown a Jablonski diagram, which can be used as a graphical reference for the following explanation.

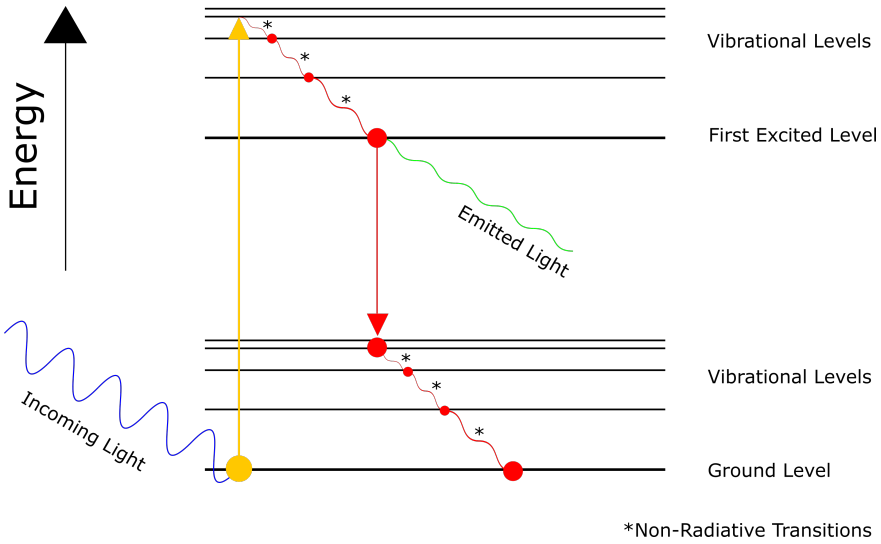

Figure 1.2: Simplified Jablonski energy diagram during a generic fluorescence process.

When a photon hits an electron, the former yields a certain amount of its energy to the latter as a result of the interaction between them. This increasing of energy can lead the molecule to occupy temporary one of the so-called excited states, in which the system is highly unstable.

The electronic state of a molecule determines the distribution of the negative charges and, according to the total electron energy and the symmetry of various electron spin

states, molecule can have many different electronic states. Each of them, can be further divided into a discrete number of rotational and vibrational sub-states, depending on the atomic nuclei and bonding orbitals. When one of these sub-level is occupied, the molecule tends to relax to the lowest vibrational energy state of the first excited singlet level, through non-radiative transitions. This process is called internal conversion, or vibrational relaxation and the energy is converted into heat. Finally, the system returns to the initial ground state, after a loss of energy. During this last step, if an emission of light took place, the molecule is called fluorescent probe, or fluorochrome, or dye; when combined with macromolecules (e.g., proteins), they are named fluorophores.

1.1.1 Fluorophores

Fluorophores are characterised according their excitation (or absorption) and emission wavelengths. Conversely to what one could think, neither absorption, nor emission spectrum is a sharp line. Indeed, both of them are bands of wavelengths and their range varies from few to hundreds of nanometres, according to the fluorophore. This feature can be explained utilizing again Figure 1.2, in addition to the Planck's Law about the energy in a *quantum*, expressed in equation 1.1:

$$E = \hbar \cdot \nu \tag{1.1}$$

When photons and electrons interact to each other, they exchange discrete amount of energy, called *quanta*. The Planck's Law tells that the frequency ν, hence the wavelength λ, of photons is proportional to their *quantum* energy E, by means of the Planck's constant $\hbar$.

Therefore, high frequency (i.e. low wavelength) photons yield high radiation energy to the fluorophores. As already stated, if the energy of the photons is high enough to allow the simplest electronic transition (from the singlet ground state to the singlet first excited level), the fluorophore gives rise to fluorescent light. Nevertheless, it does not mean that only that specific amount of energy allows fluorescence. Indeed, when higher energies are provided to fluorophores, the energy in excess is converted into vibrational and rotational energy. In other words, the system reaches high vibrational, or rotational electronic states and, very quickly, goes back to the lowest vibrational energy level of the first excited singlet state, producing heat. Lastly, it goes down further to the ground state, emitting light. Looking at Figure 1.2, it is possible to notice that the ground state has its vibrational levels, too. It means that the loss of energy of the system is not always the same, but it changes according to which vibrational state it occupies after the fluorescence phenomenon. For this reason, the emitted photons can have different energies, hence different wavelengths.

In conclusion, the excitation and emission spectra can be interpreted as probability distribution functions that a photon, with a given quantum energy, is absorbed by a fluorophore, enabling it to emit another photon as fluorescence radiation. These two spectra are also independent of each other, in the sense that no matter how much energy is given to the system: florescence emission always occurs from the lowest first excited state.

The cycle excitation - emission - relaxation can be repeated several thousands of time (according to the specific fluorophore), until the molecule is photobleached, i.e. it no longer respond to illumination.

Figure 1.3 shows a superposition of the excitation and emission spectra of GFP. This kind of graphs are useful to understand the behaviour of specific fluorophores, so that a correct imaging setup can be designed.

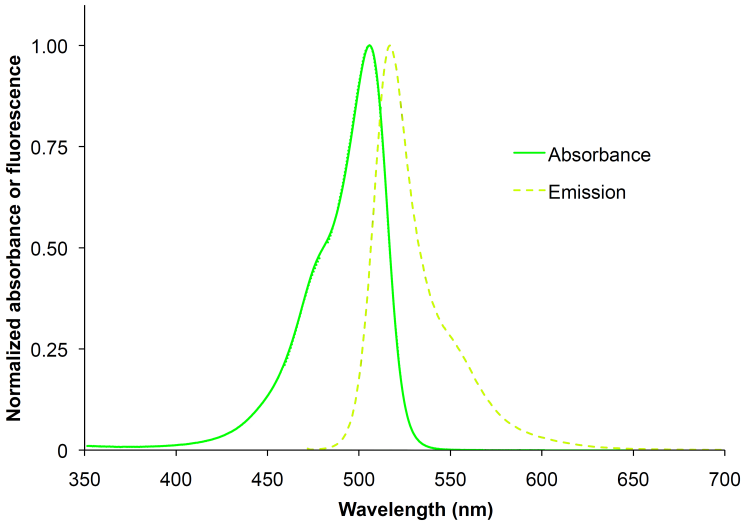

Figure 1.3: Absorption and emission spectra of GFP; peaks at 488 nm and 510 nm, respectively.

Moreover, by looking at Figure 1.4, it is also possible to extrapolate two interesting features about fluorophore properties: Mirror Image Rule and Stoke's Shift.

1.1.2 Mirror Image Rule

Both the excitation and the emission transitions end with a vibrational relaxation, in which the system return to the lowest vibrational level of the singlet state (first excited and ground, respectively). One interesting feature about the vibrational states is that the gap between them is very similar for ground and first excited states. As a result, emission spectrum is a mirror image of the absorption one. Indeed, the probability of an electron returning to a given vibrational energy level in the ground state is almost the same of the probability of having the electrode in that position before absorption.

Nevertheless, not all the fluorophores follow this rule. It is possible that, at a given wavelength, the photon yields a so high energy that a transition from the ground to the second excited state occurs, which gives rise to a local peak in the absorption spectrum. Anyway, since the system very quickly returns to the first excited level (vibrational relaxation) with non radiative transitions, that peak is not replicated in the emission spectrum.

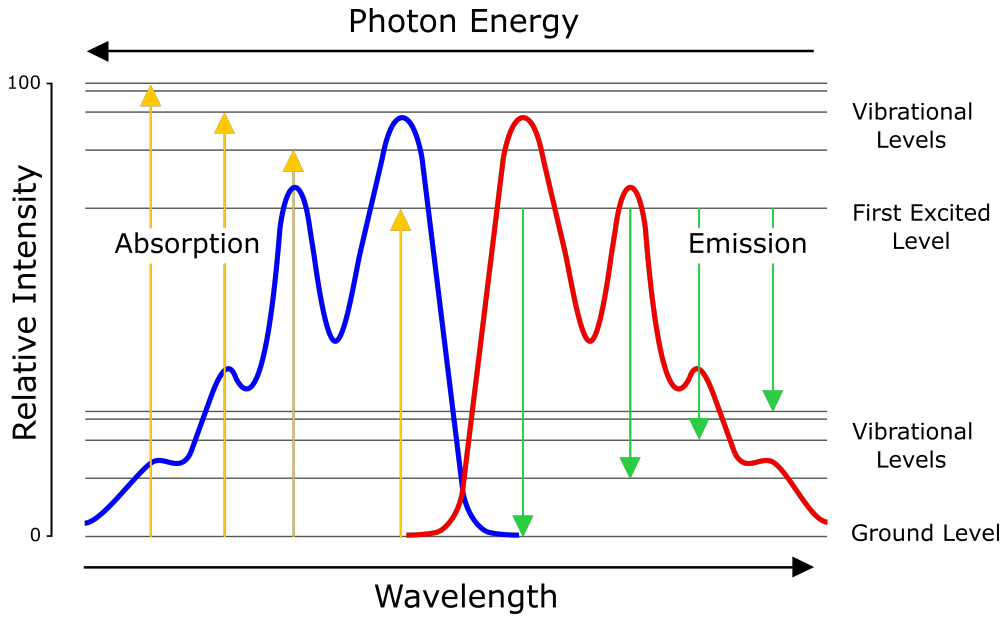

Figure 1.4: Generic absorption and emission spectra.

1.1.3 Stoke's Shift

The Stoke's Shift is one direct effect of the vibrational relaxation that electrons undergo after being excited. Indeed, as it is possible to see from Figure 1.2, as already stated, after non-radiative transition, part of the energy of the electron is converted in heat. Therefore, the emitted light has always an energy which is lower than the one yielded by the photon during the interaction photon - electron. In other words, the emitted photon has always a different wavelength (in particular longer) than the one that excites the electron; the emission spectrum is shifted to longer wavelengths and this effect is known as Stoke's Shift. It can be measured simply as the spacing between the absorption and emission peaks.

1.2 Fluorescence Microscopy

Fluorescence microscopy has become a very effective technique and, hence, largely developed and utilized. It is possible to distinguish two different fluorescence microscopy: One-Photon (1P) Microscopy and Two-Photon (2P) microscopy. Both of them share the same operating principle (see Section 1.1), but they differ in the way they exploit it.

1.2.1 One-Photon Microscopy

Also known as *Epi-fluorescence microscopy*, this technique has been improved over the years, starting from the standard optical microscopy. It exploits a light source to target and excite the fluorophores contained inside the specimen. According to the target, it is possible to choose among several light sources that are currently used in fluorescent

microscopy. They are high-pressure mercury lamps, high-pressure xenon lamps, lasers and light emitting diodes (LEDs). Each of them can be classified according to some properties such as the wavelength of the produced light and the input power, as it is possible to see in Table 1.1 [25].

Light Sources	**Wavelengths [nm]**	**Input Power**
Mercury Lamp	peaks: 313, 334, 365, 406, 435, 546, 578	100 [W]
Xenon Lamp	"uniform": 400 - 800	75 [W]
Argon Ion Laser	lines: 351, 364, 457, 476, 488, 514	50 - 100 [mW]
Helium-Neon Laser	lines: 543, 594, 633	1.5 - 10 [mW]
High-Power LEDs	from 365 to 625	1 - 5 [W]

Table 1.1: Standard light sources for 1P calcium imaging microscopy.

Other than that, price, heat production and lifetime are also other parameters very useful which have to take into account in order to understand whether a light source is close to or far from the ideal light source for fluorescence microscopy. Currently, the available light source that most closely matches the ideal one is the latest generation of high-power LED. In fact, it is characterized by a very low heat production, very long lifetime (more than 50000 hours), low price (tens of dollars, which means one or even two orders of magnitude lower than the other light sources), as well as a wide range of wavelengths, from ultraviolet (UV) up to infrared (IR).

Commercially available one-photon microscopes are able to illuminate a full microscope's field of view at once, enabling simultaneous imaging of up to a thousand individual neurons. On the other hand, such wide-field illumination leads to a decrease of image contrast, due to a background fluorescence emissions caused by the excitation of out-of-focus fluorescent molecules. Hence, an appropriate computational method is needed to extract only the firing patterns of in-focus cells [26].

Finally, it is possible to find miniaturized versions of such microscopes, which have reduced both physical dimensions and weight. Thanks to this feature, they are allowed to be head-mounted on freely behaving mice and other rodents, without affecting the quality and utility of the neural circuit data [26].

1.2.2 Two-Photon Microscopy

Also known as *Multiphoton microscopy*, this is an alternative technique to the one-photon microscopy. The phenomenon of two-photon excitation takes place when two photons are absorbed simultaneously in a single quantized event. Furthermore, the two photons must have a wavelength about twice the one required for one-photon excitation, because the energy of a photon is inversely proportional to its wavelength (recall equation 1.1). Hence, this kind of microscopy does not need a short wavelength light source, even if the resulting fluorescent emission is exactly the same obtained with one-photon excitation. Indeed, if a fluorophore normally absorbs a photon with wavelength of approximately

350 nm, then it could be also excited by two simultaneous photons of near-infrared light (about 700 nm wavelength). The Figure 1.5 represents another Jablonksi diagram which can be used to better understand this concept, by comparing 1P to 2P excitation processes.

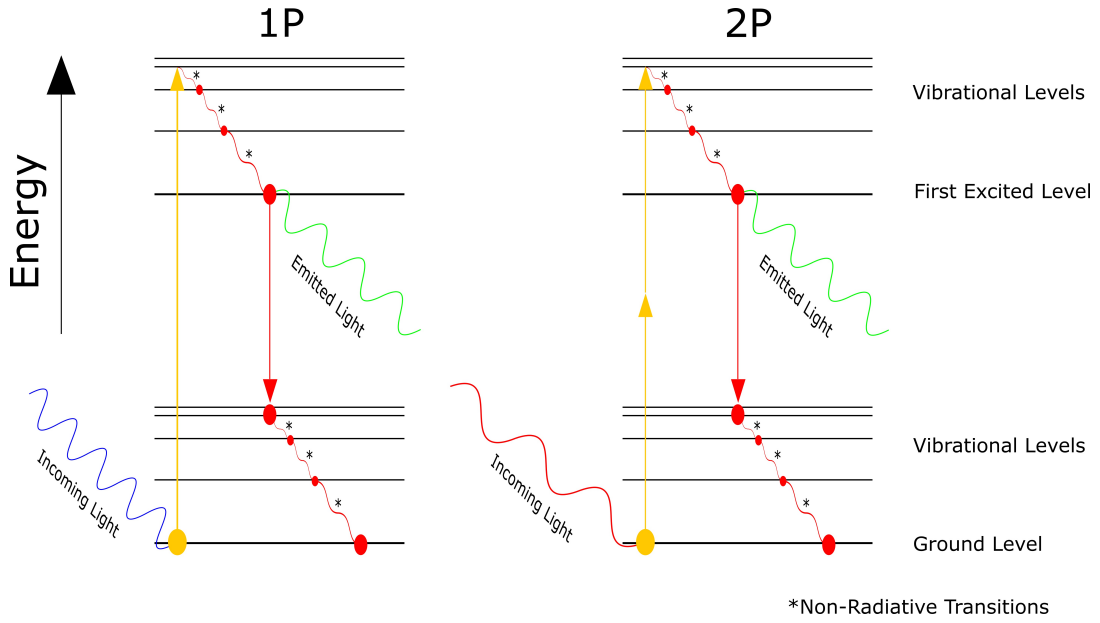

Figure 1.5: Absorption of a single photon and simultaneous absorption of two photons with longer wavelength, in a Jablonski diagram [27].

The word *simultaneous* means within an interval of about 10^{-18} seconds. As a consequence, in order to grant a sufficient number of two-photon absorption events, the photon density is about one million times greater than the one required to obtain the same number of one-photon absorptions. Thus, such a requirement may be easily achieved by using mode-locked, or pulsed, lasers, able to generate ultra-short pulses with a peak power level high enough to excite fluorophores and, at the same time, ensure a fairly low average input laser power (less than 10 mW) [28]. Nowadays instrumentation is able to generate pulses with a duration between approximately 100 fs and 1 ps and peak powers from 1 to 2 W [29].

Unlike one-photon microscopy, the microscope's focal point is confined only along the optical path where the photon flux is high enough to induce two-photon excitation. It means that, usually, a volume tissue less than 0.1 μm^3 is targeted [26]. This feature leads the laser focal spot to scan actively the entire desired field of view of the tissue. This is one of the most important advantages of this technique over one-photon microscopy: two-photon excitation only generates fluorescence at the focal plane, reducing photobleaching and phototoxicity since no background fluorescence is produced (see Figure 1.6). As a consequence, a higher number of photons is able to penetrate through the specimen, making this technique more effective at depths in thick tissues greater than what it is possible to achieve with other methods. Furthermore, the nature of the near-infrared

light (spectral range $700 - 1100\ nm$) improves the quality of in-vivo imaging, since such a light undergoes less scattering than light which has a shorter wavelength[28].

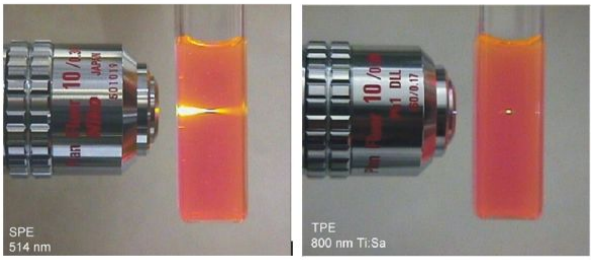

Figure 1.6: Fluorescence comparison between 1P and 2P microscopy: in the latter, photons are crowded both in space and in time, hence, only a small amount of florophores are excited [30].

On the other hand, the same feature from which such great advantages arise, is also responsible for the main drawback of the two-photon microscopy during in-vivo studies. In fact, any amount of brain motion and axial motion orthogonal to the image plane, may lead to a misalignment of image lines within the acquired image, or even to throw off the axial focal location from frame to frame in a movie. Lastly, due to the laser scanning mechanism this method has a limited number of photons per pixel and a limited imaging speed [26].

1.2.3 1P Vs 2P Microscopy

In conclusion, it is possible to make a comparison between the two mentioned techniques, in order to evaluate the one that better fits the study constraints.

Starting from the light source, as already stated before, the energy of a photon is inversely proportional to its wavelength. Therefore, while the former microscopy might need a UV light source, for the latter one a mode-locked near-infrared light source is needed. It means lower energy photons for illumination, which grants cell viability, minimizing perturbations to live thick tissue samples, (shorter wavelengths are detrimental to cells and tissues) [29]. On the other hand, in the two-photon microscopy, a much higher photon flux is required, therefore a much higher laser power is necessary. Nevertheless, by using ultrashort-pulsed lasers it is possible to maintain a low average input power.

Second, it is possible to compare qualitatively the outcome of the two. As already mentioned, the 1P microscopy is able to illuminate a full field of view at once, thus allowing simultaneous imaging of up to a thousand individual neurons, whilst the 2P excitation is based on a laser focal spot which scans the desired field of view. By comparing the two different outcomes, it is very easy to notice photobleaching in the 1P excitation, due to the background fluorescence, while it is not present at all in the case of 2P, because only the fluorophores contained in the focal plane are targeted by the photons beam. However, since the image is sampled line by line, rather than simultaneously, brain motion can lead to misalignment of image lines within the acquired image, so that motion correction could

be much harder in post-processing, which can lead to image distortions. Moreover, each pixel is sampled for a short time span (from 0.1 to 10 μs), thus a lower number of signal photons can be collected than with one-photon imaging, where each pixel is sampled for the entire duration of an image frame acquisition [26].

Lastly, they can be even compared according to how they can be applied during the experiments. In fact, commercially available miniaturized epifluorescence microscopy systems offer a device mass of only 2 grams, light enough for a mouse to easily carry during natural behaviour. This is a very important feature which makes such a system an ideal solution for complex experimental questions, without sacrificing the animal motion, social, stress, or other vital behavioural attributes. On the contrary, in a commercially available two-photon imaging systems, head fixation is currently the only possible existing way which limits the feasible applications of it. Hence, it may result as impractical, or too stressful to the animals for certain experimental scenarios [26].

Chapter 2

Acousto-Optic Technology

In this chapter, it is explained the operating principle thanks to which it is possible to obtain virtual optical waveguides and virtual relay lenses, utilizing a cylindrical piezoelectric transducer.

As already anticipated many times, a piezoelectric transducer has been used for this work. The word transducer is a general term which is given to any device capable to convert one form of energy to another one. They are nowadays largely used in applications like measurement, automation and control system and, according to their behaviour and use, they can assume several different names (e.g., optical, piezoelectric and magnetic transducer). Anyway, they can be sorted in two big categories: mechanical and electrical transducers. The former turn physical quantities into mechanical ones, while the latter turn physical quantities into electrical signals. Moreover, they can be also divided in other two groups, whether they need an external power source to be activated (passive transducers), or, on the contrary, they generate an electrical signal after being activated by an external excitation (active transducers). An example of passive transducer is an actuator. In fact, it needs an external electrical signal to operate and move or control a system, or a mechanism. On the contrary, a sensor is a typical active transducer, it converts an external stimulus to an electrical signal, used for describe the system in which it has been placed. Lastly, there are also hybrid transducers that can be behave either as an active, or as a passive transducer, according to the situation; an example is an antenna, which is able to generate radio waves from a transmitter, but also can translate electromagnetic waves into an electric signal. Another example of these hybrid transducers is the piezoelectric transducer which is described in the following Section.

2.1 Piezoelectric Transducer

The functioning of this kind of transducer is based on the piezoelectric effect, which is a particular phenomenon that can occur only on specific solid material, hence called piezo-materials. The word "piezoelectric" derives from the greek *piezein*, which means "to press", therefore it is easy to guess which are the two entities involved during the functioning of such a device. Indeed, when a mechanical stress (e.g., a compression) is

applied to a piezo-material, a potential difference can be measured across it and vice-versa; when the stress ceases (or when the structure is no more connected to an electrical source), the piezo-material comes back to its resting state. This phenomenon happens in crystalline materials (e.g., quartz) due to properties of symmetry: the tension, or the compression of such materials, lead to a displacement of the negative and positive charges, so that a net accumulation of these charges occurs along two opposite sides of the crystal structure (i.e. a variation of the charge density), as shown in Figure 2.1.

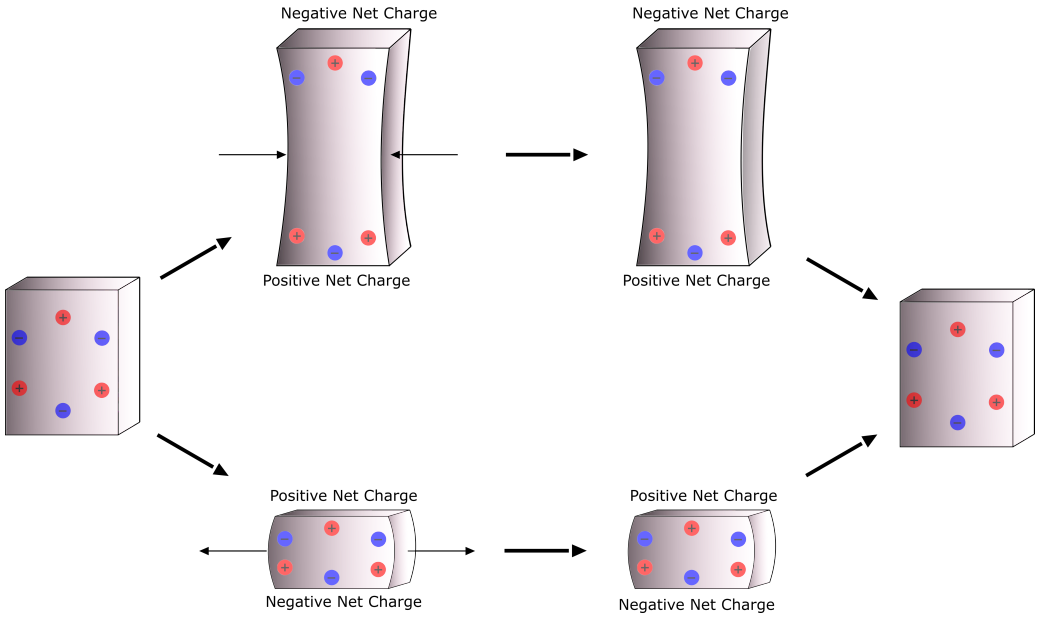

Figure 2.1: Drawing of the piezoelectric effect in a crystal: when subjected to compression, or tension, the piezo-material undergoes to a temporary physical deformation, that causes the accumulation of charges along opposite sides of the structure, hence to a potential difference across it; when the force ceases, the crystal returns to its initial resting state.

At the beginning, piezoelectric transducers were made of crystals coming from quartz, but, gradually, ceramic has become the most used material for piezoelectric transducers. There are multiple reasons behind its success. First of all, it has a high efficiency (the ratio between the energy measured at the output of the transducer and the energy given to it at the input) at low voltage; second, it can be used at high temperature, up to 300°C. Last, but not least, they are customizable, since they can be easy shaped and sized in many different ways. In fact, according to their thickness, it is possible to design the piezoelectric vibration frequency: a thin element vibrates with a frequency that is twice its thickness. Hence, the higher the desired frequency, the thinner the active element.

According to how a piezo-material is cut, it is possible to distinguish among three different operational modes [31]:

Transverse effect

The amount of charge, displaces among the direction perpendicular to the line of force, depends on the geometrical dimensions of the piezoelectric element:

$$C_x = d_{xy} \cdot F_y \cdot b/a \tag{2.1}$$

Longitudinal effect

Conversely to the previous one, the displaced charge is strongly proportional to the applied force, whilst independent of the size and shape of the piezoelectric element. It is possible to increase the charge, only by putting several elements mechanically in series (i.e. electrically in parallel):

$$C_x = d_{xy} \cdot F_y \cdot n \tag{2.2}$$

Shear effect

Same as for longitudinal effect, for n elements, the charge displaced is:

$$C_x = 2d_{xy} \cdot F_y \cdot n \tag{2.3}$$

where, x indicates the direction normal to the force F, which is along y; a and b are the dimension in line with y and x axes, respectively; n is the number of elements and d_{xy} is the corresponding piezoelectric coefficient, depending on the material.

2.2 Cylindrical Piezoelectric Transducer

In Figure 2.2 a drawing of the hollow cylindrical transducer is shown. It is radially polarized and the electrodes are connected to the internal and external of the cylindrical surface. For convention, the inner one is the positive, while the external is the negative electrode. Such a geometry, allows the transverse piezoelectric effect to obtain axial, radial and lateral displacements (see Figures 2.3a, 2.3b and 2.3c [32]).

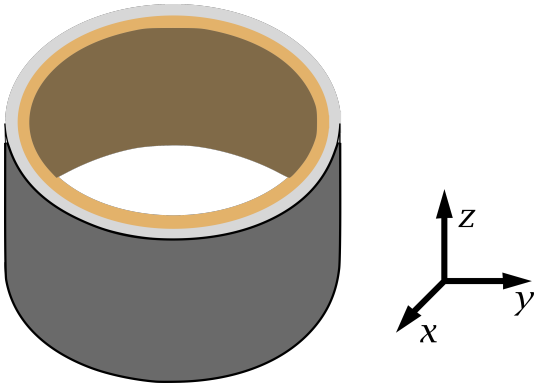

Figure 2.2: Drawing of the cylindrical piezoelectric transducer.

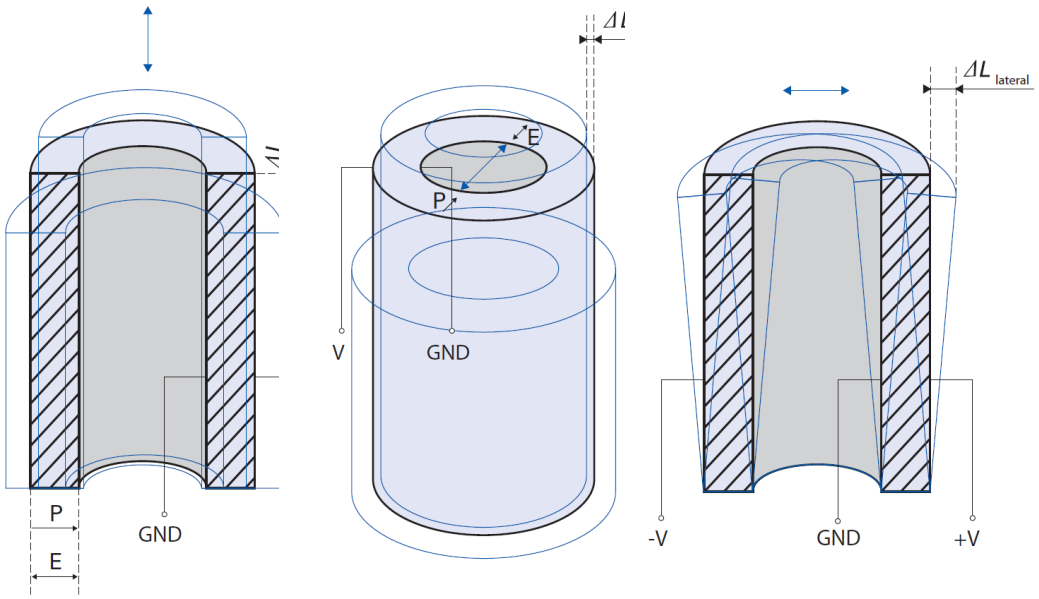

(a) Axial displacement (b) Radial displacement (c) Lateral displacement

Figure 2.3: Possible displacements in the transverse piezoelectric effect; P is the direction of polarization and E the electric strength.

2.2.1 Electromechanics

There are many relationships and coefficients that governs the behaviour of polarized piezoelectric materials. In this section, it is shown a simplified form of the basic connection between electrical and mechanical properties in a cylindrical piezo-transducer. Such a relationship applies only to little electrical and elastic amplitude values (i.e. small signal values). In that range, the equations are linear, with constant coefficients:

$$\begin{cases} D = d \cdot T + \epsilon^T \cdot E \\ S = s^E \cdot T + d \cdot E \end{cases} \tag{2.4}$$

where D stands for the electric flux density, d is the piezoelectric charge coefficient, T is the mechanical stress, ϵ^T is the permittivity (for T constant) and E the electrical field; S is the mechanical strain and s^E is the compliance or elasticity coefficient (for E constant) [32]. For a detailed explanation of those formulas, see [33][34].

We assume that we can apply to the transducer a driving voltage frequency and amplitude so that:

$$V = V_a \cdot sin(\omega t) \tag{2.5}$$

with $\omega = 2\pi f$, the angular frequency and V_a the voltage amplitude. Therefore, it is possible to obtain a relation between the applied voltage and the displacement for each

axial (2.6), radial (2.7) and lateral (2.8) effects [32][35]:

$$\Delta L_{axial} = \frac{d_{31} \cdot l}{t} \cdot V \tag{2.6}$$

$$\Delta L_{radial} = d_{31} \cdot \frac{ID + t}{2t} \cdot V \tag{2.7}$$

$$\Delta L_{lateral} = 0.9 d_{31} \cdot \frac{l^2}{(ID + t)t} \cdot V \qquad for\ ID >> t \tag{2.8}$$

where l is the height of the transducer, t is its thickness and ID the internal diameter.

Resonance

The cylindrical piezoelectrical transducer is able to change its dimensions cyclically (due to vibrations), when driven by an AC electrical signal. Moreover, according to the signal frequency, the transducer converts the electrical energy into mechanical vibrations differently. The frequency at which the piezo-element reaches the highest efficiency in terms of energy conversion is called resonance frequency. The resonance frequency of a given piezoelectric transducer depends on its size and on the vibration mode; it can be evaluated by:

$$f_{r-axial} = \frac{1}{2\tau_r \sqrt{\rho \cdot s_{33}^D}} \tag{2.9}$$

$$f_{r-radial} = \frac{1}{\pi d_{mr} \sqrt{\rho \cdot s_{11}^E}} \tag{2.10}$$

$$f_{r-lateral} = \frac{1}{2\omega_r \sqrt{\rho \cdot s_{11}^E}} \tag{2.11}$$

where, $d_{mr} = (d_{outer} + d_{inner})/2$ is average diameter, $w_r = (d_{outer} - d_{inner})/2$ is the average thickness, ρ is the density, t_r is the height of the transducer, s_{11}^E is the elastic coefficient (for E constant) and s_{33}^D is the elastic coefficient (for constant charge density) [36]. From the electrical point of view, the resonance frequency has an impact on the impedance of the piezo-element. In fact, it is the frequency at which the series resistance in the equivalent electrical circuit is zero, ignoring the resistance due to mechanical losses. There is also the anti-resonance frequency, which has the opposite effect of the resonance frequency: the parallel resistance in the electrical circuit is infinite (again, ignoring the mechanical losses).

Furthermore, increasing the frequency of the electrical signal, it is possible to notice that the transducer undergoes this behaviour periodically. In fact, the equations (2.9) - (2.11) are referring to the fundamental resonance frequency; by multiplying the fundamental one by any integer value, it is possible to obtain again the same resonance effect.

The equations (2.6) - (2.8) are valid only for working frequencies below than the piezoelectric first resonant frequency. For frequencies equal to, or greater than that, here it

is possible to find the other solutions [37] that are not reported here, since the purpose of this section is just to give to the reader a basic knowledge about the relationships between voltage, displacement and pressure in a hollow piezoelectric transducer.

2.2.2 Acoustic Waves within the Cavity

When the walls of the ceramic cylindrical piezoelectric transducer vibrate, acoustic waves propagate inside its cavity, through the medium, generating standing-pressure waves. Their propagation can be studied starting from the one-dimensional vibration case and then extend the physics in a two and three-dimensional waveguide [38].

One-Dimensional Vibration

The standard approach to the study of vibrations in such a geometry, is the analysis of a string.

A string, stretched with a certain tension and then released, can oscillate between two points changing its shape according to the frequency of oscillation, the tension used to pull the string and the boundary conditions. In fact, the behaviour of the string changes whether the two end of the string are fixed, or not.

Starting from the first boundary conditions, it is possible to write the equation which describes the displacement of the string:

$$y_n(x,t) = Asin(k_n x)e^{-i\omega_n t}, \quad k_n = \frac{n\pi}{L}, \quad \omega_n = k_n c \tag{2.12}$$

where k_n is the wave number, $\omega_n = 2\pi f_n$ the angular frequency, L is the length of the string, or the distance between the two point at which it is fixed; $n = 1,2,...$ is an integer number which describes the basic shapes, called *modes*, that give rise to the vibration of the string (Figure 2.4).

$\omega_n = k_n c$ is called *dispersion relation* and put in relation vibration frequency with the wave number, hence, the mode. Therefore, each mode has its own oscillation frequency and higher modes have higher frequencies.

Furthermore, it is possible to rewrite the equation (2.12) by substituting the sine function by its complex representation: $sin(x) = \frac{e^{ix}-e^{-ix}}{2i}$, obtaining:

$$y_n(x,t) = \frac{A}{2i}(e^{i(k_n x-\omega_n t)} - e^{-i(k_n x+\omega_n t)}) \tag{2.13}$$

the (2.13) equation represents the displacement of the string as a superposition of two waves propagating in opposite directions, one to the right ($+x$) and one to the left ($-x$), at speed c.

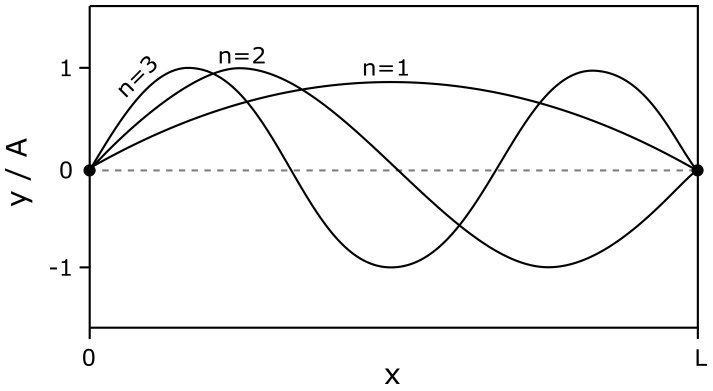

Figure 2.4: The first three modes, or harmonics, for a string which vibrates with fixed ends.

Similarly, for a non-fixed string, it is possible to rewrite the equation (2.12) as:

$$y_n(x,t) = Acos(k_n x)e^{-i\omega_n t} \tag{2.14}$$

and, again, it is also possible to write it as the superposition of two propagating waves, since $cos(x) = \frac{e^{ix}+e^{-ix}}{2}$:

$$y_n(x,t) = \frac{A}{2}(e^{i(k_n x-\omega_n t)} + e^{-i(k_n x+\omega_n t)}) \tag{2.15}$$

Even if $n = 0$ gives a mathematical displacement, it has no physical meaning (Figure 2.5).

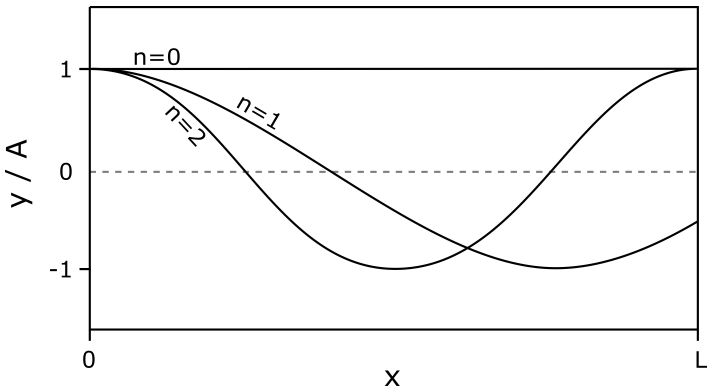

Figure 2.5: The first three modes, or harmonics, for a string which freely vibrates

Two-Dimensional Vibration

As already mentioned, it is possible to extend the 1D-string vibration theory to a 2D structure and, therefore, describe the behaviour of an acoustic wave inside a waveguide with rigid walls, like a cylindrical piezoelectric transducer. This time, the boundary

condition to apply is that there is no displacement outside the walls, i.e. the gradient normal to the wall is zero.

Consider acoustic wave as a plane wave which is propagating with an angle θ with respect to the axial direction of the waveguide. In this case, the propagation undergoes multiple reflections between the two rigid walls. It is possible to easily quantify the displacement of the phase front of each reflected plane wave: assuming c as its speed, then, after a Δt interval, it will be moved by a quantity equal to $c\Delta t$.

In a plane wave under this conditions, it is possible to distinguish among two different speeds: the *phase velocity* and the *group velocity*. The latter refers to the speed of the phase front of the wave generated by the superposition of each reflected wave; the former is the axial component of the speed at which each wave is propagating inside the waveguide. Hence, $c_g = c \cdot cos(\theta)$, while $c_p = \frac{c}{cos(\theta)}$ (see Figure 2.6).

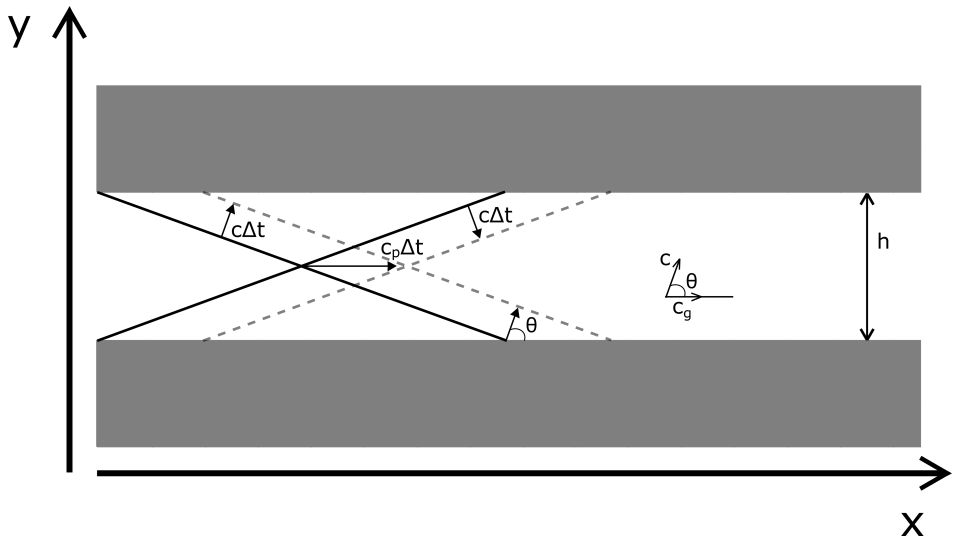

Figure 2.6: Acoustic wave propagating along the axial direction, within a 2D waveguide, with an angle θ with respect to the rigid walls. Solid lines indicates the positions of the phase fronts at $t = t_0$, while the dashed lines indicates the positions after the Δt interval.

Similarly to the 1D case, (2.16) expresses the displacement for the two plane waves, while (2.17) is given by the superposition of the two:

$$p_{\pm}(x, y, t) = \frac{A}{2} e^{i(k_1 x \pm k_2 y - \omega t)}, \quad k_1 = kcos(\theta), \quad k_2 = ksin(\theta), \quad \omega = kc \tag{2.16}$$

$$p(x, y, t) = Acos(k_2 y) e^{i(k_1 x - \omega t)} \tag{2.17}$$

where p_+ and p_- are the plane waves which propagate upward $(+y)$ and downward

$(-y)$, respectively. Applying the boundary condition at the edges $y = 0$ and $y = h$:

$$\frac{\partial p(x,y,t)}{\partial y} = 0 = -k_2 A sin(k_2 y) e^{i(k_1 x - \omega t)} \tag{2.18}$$

this condition is satisfied for

$$k_2 = \frac{n\pi}{h}, \quad n = 0,1,2... \tag{2.19}$$

Conversely to the 1D analysis, this time $n = 0$ has a physical meaning and it can be understood through the description of the dispersion relation. From (2.18), by substituting $k = \sqrt{k_1^2 + k_2^2} = \frac{\omega}{c}$, it is possible to write the dispersion relation as follows:

$$f_n(k_1) = \frac{c}{2\pi}\sqrt{k_1^2 + (\frac{n\pi}{h})^2} \tag{2.20}$$

From equation (2.16), it is possible to obtain the formula which describes, for each mode, the angle of the plane waves inside the waveguide:

$$\theta_n(f) = arcsin(\frac{nf_0}{f}), \quad f_0 = \frac{c}{2h} \tag{2.21}$$

In summary, from the equations (2.20) and (2.21), it is possible to say that the propagation of an acoustic plane wave, within a waveguide with rigid walls, is characterized by having an infinite possible number of modes, according to the frequency of the wave itself. Indeed, each mode can be triggered by its minimum frequency (*cut-on frequency*) evaluated by the equation (2.20), except for the $n = 0$ mode, which exists for all the frequencies. This particular mode, represents the acoustic plane wave which propagates through the waveguide, without any reflections ($\theta_n(f) = 0$ from (2.21)). Anyway, for all the modes greater than $n = 0$, at the cut-on frequency, a standing wave inside the waveguide is formed, without any propagation. Indeed, at this condition, the group velocity is zero and the phase velocity is infinite (i.e. $\theta_n(f) = 0$). Thus, it is possible to say that the phase front of the structure moves at the phase velocity, whilst the energy of the plane wave progresses at the group velocity.

Three Dimensional Vibration

Furthermore, it is possible to extend the 2D acoustic wave propagation to a 3D, infinitely long cylinder, with rigid walls and filled with a fluid. The difference, with respect the previous 2D case, is that there are two numbers, m and n, that identify each mode inside the cavity (Figure 2.7): the latter is called angular number due to its angular dependence ($cos(m\theta)$) and it refers to the nodal lines through the centre of the waveguide; the former indicates the number of nodal circles and it is called radial number, due to its radial dependence ($J'_n(\frac{\alpha_{mn} r}{a})$, where r is the radial distance, a the radius of the cylinder, α_{mn} a constant which depends on the specific mode, and J'_n is the derivative of a Bessel function). Again, each mode has a cut-on frequency and only the $(m, n) = (0,0)$ mode exists at all frequencies.

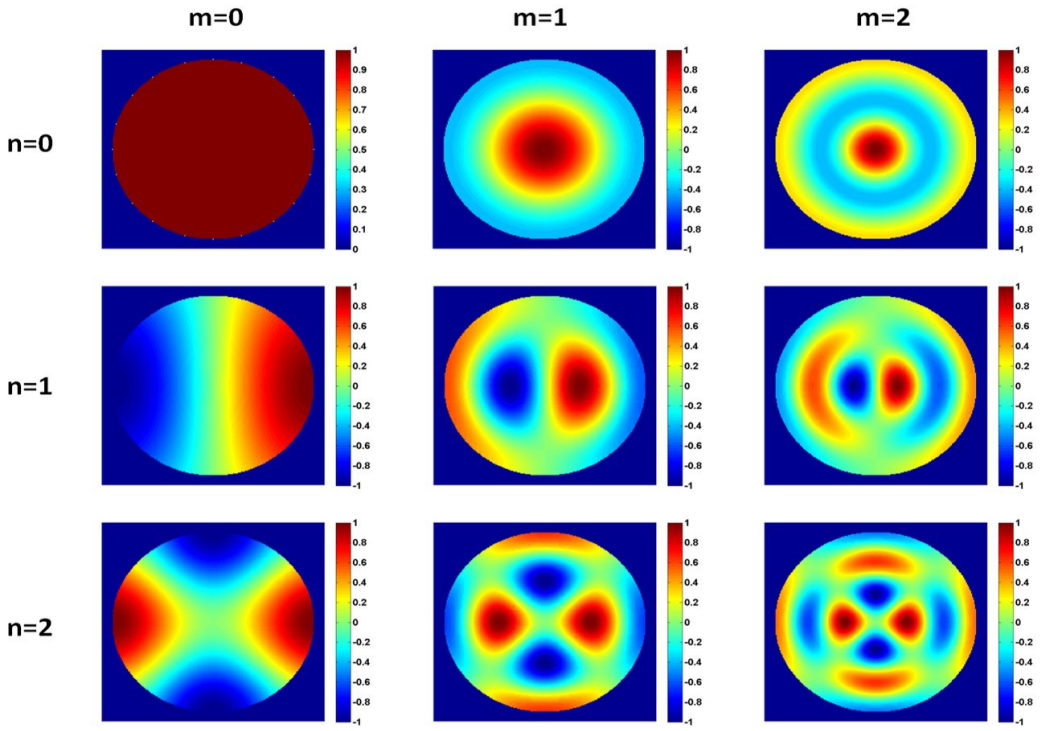

Figure 2.7: First 9 modal structures in a filled cylindrical piezo-transducer, with rigid walls; the pressure intensity is shown with normalized units [38].

2.2.3 From Pressure to Refractive Index

In Sections 2.2.1 and 2.2.2, it has been shown that, when a ceramic cylindrical piezoelectric transducer, radially polarized, is driven by a sinusoidal voltage, standing-pressure wave are generated inside the cavity, stimulated by the electromechanical vibrations. Here, it is shown that these pressure waves are able to modulate the refractive index of the medium within the cavity.

In fact, the acoustic-pressure distribution inside the cylinder, in the simplest radial mode ($n = 0$) is the following [39]:

$$\Delta p(r,t) = p_1 J_0(\frac{\omega r}{v}) sin(\omega t) \tag{2.22}$$

where p_1 represents the amplitude of the acoustic pressure, J_0 is the $0th$ order Bessel function of the first kind, v is the speed of sound in the acoustic medium.

Moreover, it is possible to put in relationship pressure and density of the medium. Indeed, ultrasonic pressure waves directly modulate density, since the medium is compressed in the high-pressure regions resulting in a higher dense state, while it is rarefied in the negative pressure areas, where the local density is reduced. Furthermore, the change of the density, has a direct effect on its refractive index. In fact, since the variations of

density is small, it is possible to use the linearised version of the Lorentz-Lorenz equation:

$$n = n_0 + n_a J_0(\frac{\omega r}{v}) sin(\omega t) \tag{2.23}$$

where n_a is the perturbation pressure-dependant refractive index [40].

This is a very important result, because it puts the basis for the concept of the virtual acousto-optic waveguide. In fact, focusing on the equation (2.23), it is clear that the refractive index of the medium changes locally, following the same behaviour of the density and, therefore, of the pressure profile. Figure 2.8 illustrates the shape of such refractive index in an hypothetical medium. By taking the difference between its maximum (positive pressure/density peaks) and minimum values (negative pressure/density troughs), it is possible to analyse the local refractive index contrast; if high enough, the cylindrical piezoelectric transducer can behave as a virtual optical waveguide, hence, confining light within the medium.

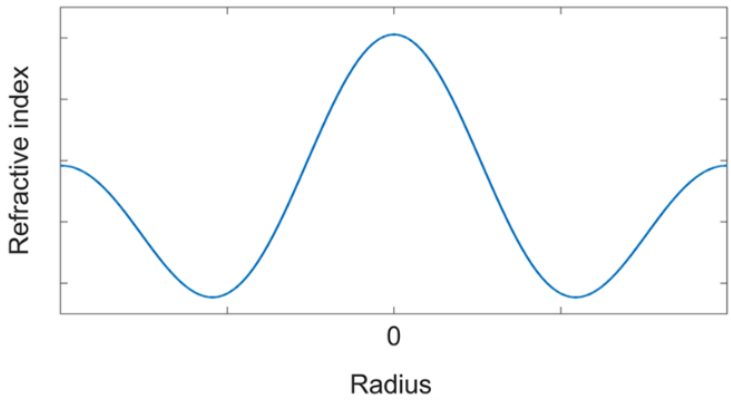

Figure 2.8: Refractive index distribution of an hypothetical medium inside the cylindrical piezoelectrical transducer. As expected, the maximum value is exactly in the centre of the cavity ($r = 0$), since it is also the point of maximum pressure and density, due to ultrasonic standing-pressure waves [41].

2.3 Virtual Optical Waveguide

In order to better understand the last sentence of Section 2.2.3, a brief description of the operating principle of optical waveguides (i.e. optical fibre) is provided here.

Optical fibres generally consist of an inner material in which light travels (core), surrounded by an outer component (cladding) which acts as a barrier that limit the light travelling only inside the core. This mechanism is based on the refractive index contrast between the core and the cladding. Indeed, when the core has a higher refractive index with respect to the cladding, from the Snell's Law, it is possible to obtain the so-called *critical angle*, which allows the propagation of light by total internal reflection. This is what happen in the so-called *step index* fibre. Similarly, the propagation of the light

inside the waveguide can be obtained in a structure in which the refractive index gradually changes along the radial direction. These optical fibres are called *Graded Index* (GRIN). In this case, the light, instead of undergoing multiple reflections at the edge core-cladding, is steered continuously along the axial direction, in a sinusoidal-like shape propagation (see Figures (2.9a - 2.9b).

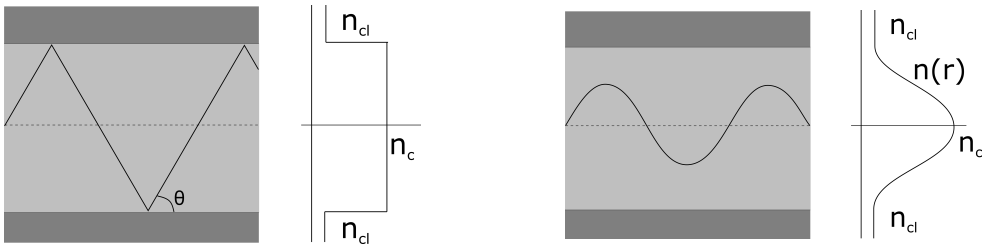

Figure 2.9: Propagation of light in (a) step-index and in (b) GRIN optical fibre.

At this point, by comparing Figure 2.8 with 2.9b it should be clear that the cylindrical piezoelectric transducer is able to replicate the behaviour of a GRIN optical fibre, when the refractive index contrast of the medium (i.e. $n(r)$) is so high that the transducer generates a virtual core-cladding structure within its cavity.

Having said that, there is an important difference between the two and it refers to the optical properties of the employed medium. In fact, a GRIN optical fibre is made of minimally scattering materials, whereas the virtual waveguide has optical properties that belongs to the medium which fill the cavity of the cylindrical transducer. Since this technology is thought to be used in tissue, they are scattering medium. As a result, the propagated modes undergoes larger loss of energy, with respect to GRIN optical waveguides.

Lastly, it is important to highlight that the behaviour of such a virtual optical fibre can be tuned in real-time. Indeed, by recalling the relationship sinusoidal voltage - vibrations - displacement - acoustic waves - ultrasonic standing-pressure waves - density - refractive index, it is possible to say that a simple change on one of these parameters triggers a domino effect, which ends up modulating the refractive index of the medium. This parameter can be put in relation with another one that describes the ability of optical waveguides in propagating light: the numerical aperture (NA). In general, this parameter can be defined as a dimensionless number, related to the range of angles over which an optical system can accept or emit light [42]. In the case of optical fibres, it can be defined as follows [43]:

$$NA = \sqrt{n_{core}^2 - n_{cladding}^2} \tag{2.24}$$

In other words, this number describes the ability to reduce the scattered light within the scattering medium. High numerical aperture means that the virtual waveguide is able to recollect, and therefore, confine a higher amount of scattered light along the centre of the transducer. Hence, by increasing the refractive index contrast, it is possible to improve the efficiency of the virtual optical fibre, by guiding and confining light through

an optically thick scattering tissue [41]. This result can be achieved simply by increasing the AC signal voltage amplitude applied to the transducer, as shown in Figure 2.10:

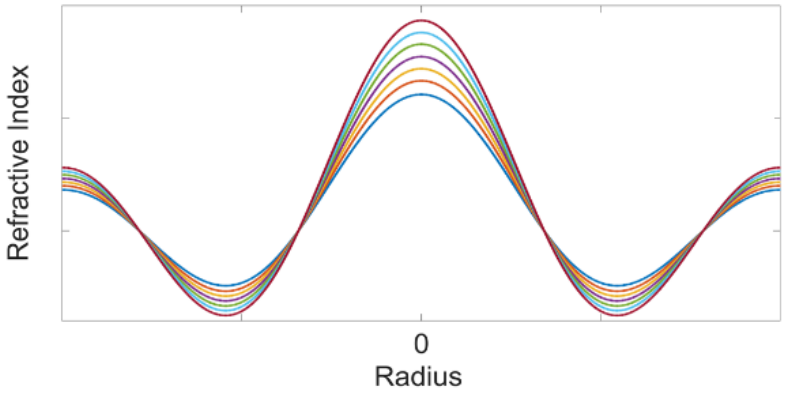

Figure 2.10: Effect of voltage amplitude to the refractive index contrast within the medium: increasing the voltage, the refractive index contrast increases, and vice-versa. As a consequence, higher voltages grant greater NA of the virtual optical fibre [41].

In this way, it is possible to obtain a non-invasive virtual optical fibre, able to guide and confine light within a scattering medium, with a penetration depth of light way greater than the one achievable in standard one-photon calcium imaging microscopy, which allow neuron interrogation/stimulation in deeper regions, impossible to reach with other non-invasive methods.

2.4 Virtual Relay Lens

The Section 2.3 ended talking about NA in optical fibres. This parameter is also widely used in optics, in order to describe and assess lenses. Figure 2.11 can be used in order to better understand the physical meaning of some of their features. The purpose of this Section is to provide a basic knowledge about some lens properties, in order to let the reader able to understand the application of the cylindrical piezoelectric transducer as a virtual relay lens.

Given n the refractive index of a medium in which a lens is placed, the cone of light entering or exiting the lens can have a maximum half-angle θ. Therefore, the numerical aperture of the lens can be written as:

$$NA = n \cdot sin(\theta) \tag{2.25}$$

A lens can be assessed also through other parameters, like the shape (e.g., concave, convex,...), the focal distance and the size (i.e. the diameter). The focal length, as shown in Figure 2.11 is defined as the distance at which a lens focuses the entering/exiting light, or, in other words, the distance between the lens and the focused plane, or image.

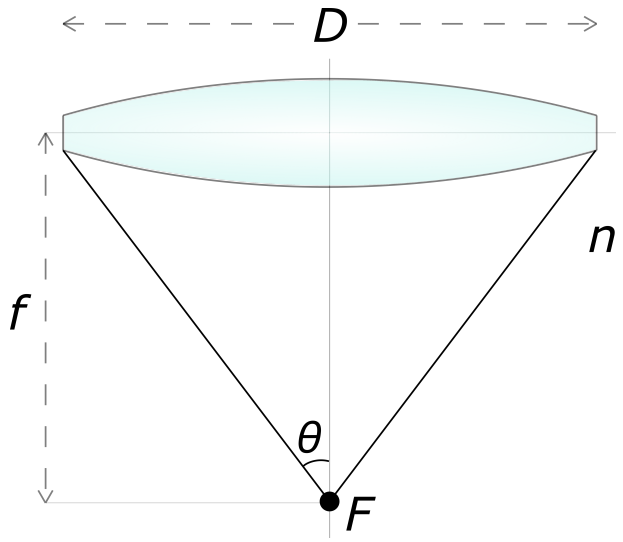

Figure 2.11: Drawing of a bi-concave thin lens. F is the focused point, placed at a distance equal to f (i.e. focal length) from a lens which has a diameter D. θ is the maximum half-angle of the cone of light that can enter/exit the lens and n (not showed) is the refractive index of the medium which surround the lens.)

From Figure 2.11 it is possible to write θ as

$$\theta = arctan(\frac{D}{2f}) \tag{2.26}$$

For small values, it is possible to approximate $arctan(x) \approx x$. Therefore, by substituting equation (2.26) in (2.25):

$$NA = n \cdot sin(\theta) \approx n \cdot \frac{D}{2f} \tag{2.27}$$

Hence, focal length and NA of a lens are inversely proportional and both of them depends on the refractive index.

As stated in Section 2.3, thanks to the acousto-optic technique, it is possible to modulate the refractive index of the medium. Therefore, other than a virtual GRIN optical fibre, the transducer itself can be seen also as a GRIN lens and, moreover, with a tunable focal length. As a result, this last feature allows to change dynamically the focal length of a lens, hence the working distance of zoom, or objective lenses (see Figure 2.12).

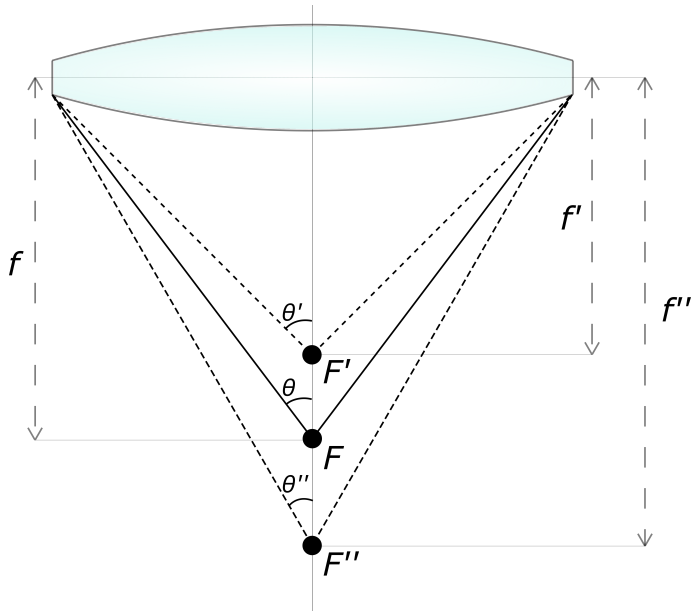

Figure 2.12: Drawing of the effect of NA on the focal length of a lens: given a refractive index of the medium n, a lens, with a focal length f, is able to get the focal point F in focus. By increasing the refractive index, a new focal length F'' is obtained; on the contrary, a decrease of the refractive index leads to F'.

Chapter 3

One-Photon Microscope

In Section 1.2.1, a general overview of 1P microscopy has been provided and lastly compared to the 2P. On the contrary, the goal of this chapter is to describe more in detail each component of this microscopy, providing information about the setup that has been designed and built for this thesis.

In this kind of microscopy, the specimen is targeted by a light, which is able to excite the fluorophores within the sample, so that a microscope collects and show the emitted light. According to this brief description of the operating principle, it is possible to outline all the necessary components for a 1P microscope. They are:

- light source;
- excitation and emission filters;
- objective;
- camera.

Other than those listed above, it is necessary to take into account also all the lenses and mirrors needed for the optical path, which change according to the microscope.

3.1 Light Source

The choose of the light source is strictly related to the experiment that has to be performed, since it must be compatible with the fluorophores of the specimen. Recalling Table 1.1, it is possible to distinguish among two different categories of light sources: broadband (i.e. lamps) and single wavelength (i.e. lasers and LEDs).

Light Sources	**Wavelengths [nm]**	**Input Power**
Mercury Lamp	peaks: 313, 334, 365, 406, 435, 546, 578	100 [W]
Xenon Lamp	"uniform": 400 - 800	75 [W]
Argon Ion Laser	lines: 351, 364, 457, 476, 488, 514	50 - 100 [mW]
Helium-Neon Laser	lines: 543, 594, 633	1.5 - 10 [mW]
High-Power LEDs	from 365 to 625	1 - 5 [W]

Table 3.1: Standard light sources for 1P calcium imaging microscopy.

The advantage of lamp light sources is that, since they can have a very large emission spectrum, can be used to excite different fluorophores, even during the same experiment. However, it could happen that such light source has a low emission energy at the wavelength of interest, leading to a weak fluorescence. On the contrary, lasers or LEDs can be chosen according to the wanted wavelength, so that their emission spectrum coincides with the absorption one of the targeted fluorophore, maximizing the fluorescence intensity. On the other hand, if multiple fluorophores must be triggered during the experiment, it must be add one light source for each of them. Therefore, there is a trade-off between the versatility of the source and the efficiency of the fluorescent process.

3.2 Filters

Once selected the light source, it is necessary to choose the correct filters for the experiment. They are characterised by the reflection and transmission bands, since their goal is to cut off undesired wavelenghts, allowing only a small range of it to pass through them.

They can be divided into excitation and emission filters; however, not all the microscopes have both of them. Indeed, while the emission one is always required, the excitation filter can be useless when a single wavelength light source is employed. On the contrary, in case of using a lamp, it is mandatory in order to select only a specific small range of allowed wavelengths, avoid excitation of other sources of fluorescence. The emission filter, as anticipated, is mandatory in any case for two main reasons. The first one is due to the fact that the excitation light is always stronger than the emitted one; it means that, without this filter, the camera would not be able to see any fluorescent light, since it would be darken by the excitation light. The second one is related to the background illumination of the sample, that would reduce the contrast between the fluorescent neuron and the surrounding tissue. Both of these two issues are easily solved by placing an emission filter, before the camera, able to select only a small range of allowed wavelengths, centred on the emitted wavelength of the specific fluorophore.

3.3 Objective

The task of this component is to collect light from the sample being observed, in order to produce the real image at a fixed distance behind it, by focusing the entering light rays (see Figure 3.1). This real image can be observed directly through an eyepiece, or recorded by a camera sensor. Usually, objectives consist of many optical components (i.e. lenses), which are responsible for its optical features (e.g., working distance, magnification factor, NA, quality correction,...), as well as physical features (e.g., length, pupil diameter). For this reason, it can be stated that objective are the most complex component in a microscope.

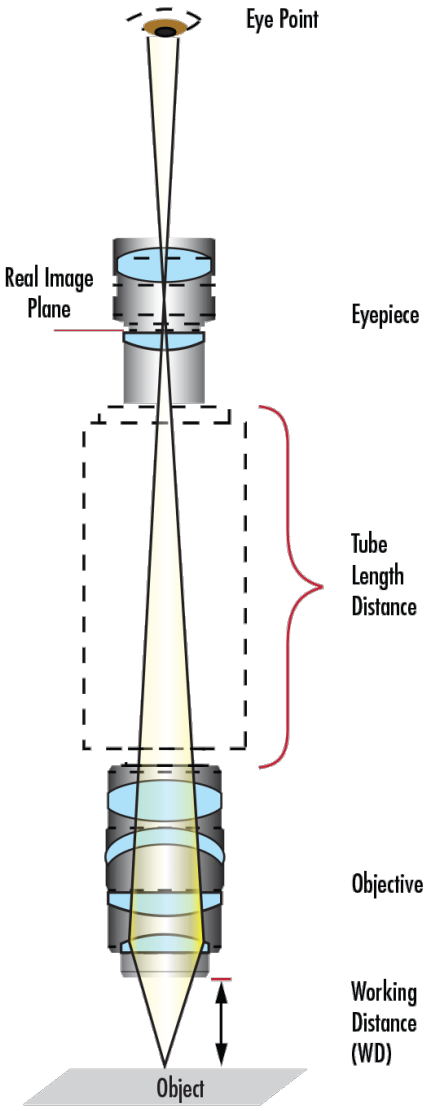

Figure 3.1: Drawing of the optical path in a general objective-eyepiece system microscope. The eyepiece can be replaced by a camera sensor [44].

The correct choice of the objective, can dramatically change the quality of the imaging carried out by the microscope. However, it is always useful not focusing only on the objective alone, but it should be considered the complete system performance.

An optical system can undergo many different optical aberrations which cause a detrimental effect in terms on the imaging quality. In fact, aberrations lead to a produced real image which is distorted, or blurred, according to the type of occurred aberration. Technically, it happens when the light is not focused on one single point, but, on the contrary, it is spread over a larger area.

Aberrations can be divided into two categories: monochromatic and chromatic. The former is related to the optical geometry of the system (e.g. mirrors and lens), whereas the latter is due to the dispersion of light, i.e. different wavelengths propagates in different directions, hence are focused at different points.

To reduce the effects of aberrations, it is possible to find achromatic, apochromatic, plan and semi-plan objectives. The first two reduce the chromatic aberrations at multiple wavelengths, while the second two reduce the field curvature effect; it happens when the focus of the lens is on a curved surface rather than a plane, causing a blurred image. For the purpose of this work, the objective needs to collect only the fluorescent light emitted by the fluorophores, hence chromatic aberrations have not to be considered.

The working distance (WD) of the objective indicates the distance at which the objective must be place in order to get the specimen in focus. Since it is the result of the focal lengths of the lens system contained inside the objective, this parameter is strictly related to the numerical aperture (recall equation (2.27)). In fact, by increasing the WD, the half-angle of the cone of light that enters the objective is reduced. When a very high NA is wanted (greater than 1), immersion oils can be applied between the objective and the specimen, so that the refractive index of the medium is increased ($n_{air} = 1$, $n_{oil} = 1.5$), giving a higher NA (recall equation (2.25)). The same relationship is also valid for the magnification.

Working distance of objectives can vary from less than 1 mm up to tens of cm. The last case belongs to the very long working distance objectives ($VLWD$), used in stereomicroscopes.

Lastly, the magnification is also related to the field of view (FOV), which is the parameter that describes the area imaged by the microscope. It slightly changes when an eyepiece is used instead of a camera sensor. Indeed, when using an eyepiece, the real image can be further magnified by the eyepiece itself. Anyway, even when a $1X$ eyepiece is used, the FOV is still different in the two systems and it is due to the difference between the camera sensor and the eyepiece shapes. A camera sensor has a rectangular shape, meaning that a portion of the image relayed to the camera is cut off. On the contrary, the eyepiece is circular, therefore it is able to capture all the full FOV given by the objective. Hence, it is possible to write:

$$FOV_{camera-objective} = \frac{Camera\ Sensor\ Size}{M_{objective}} \tag{3.1}$$

$$FOV_{eyepiece-objective} = \frac{Field\ Stop_{eyepiece}}{M_{objective} \cdot M_{eyepiece}} \tag{3.2}$$

where M stands for magnification factor and the $Field\ Stop_{Eyepiece}$ indicates the entrance pupil diameter of the eyepiece.

3.4 Camera

The camera, as well as the objective, is a critical component of a microscope, therefore, the choice of the right one always takes time, due to all the necessary trade-offs between its parameters [45].

A first distinction among all the possible camera on the market is about its technology. In fact, it is possible to distinguish between charge-coupled device (CCD) and complementary metal-oxide semiconductor ($CMOS$) cameras. Without going too deep into the details related on the technology (and then losing the purpose of this section), it is possible to analyse the difference between the two in terms of imaging.

The operating principle of a digital sensor camera is converting each photon, that hits the photodiodes onto the chip, into an electron (even called *photoelectron*); after a fixed time, i.e. the exposure time, that can be set according to the needs, the amount of the stored photoelectrons will corresponds to a grey value, pixel by pixel. The difference between CCD and CMOS is in the way they read the number of photoelectrons obtained by the photodiodes. Indeed, the former has an unique amplifier and analog-to-digital converter (ADC) for all the photoelecrodes packets, whereas the latter has multiple ADCs (one for each column of the sensor) and, moreover, each photodiode has its own amplifier. Of course, this leads to advantages, but also disadvantages in both of the cases. In fact, if on one hand a CCD camera is able to expose each pixel of its sensor for the same amount of time (i.e. *Global Shutter*), on the other hand it needs to wait that all the charge packets are sent and digitized by the same ADC, before starting a new exposure, meaning a reduced frame rate. On the contrary, a CMOS camera can process each pixel of an entire row at a time and, instead of waiting that all the rows have been digitized, as soon as one row is sent to the ADCs, it starts a new exposure for the next frame (i.e. *Rolling Shutter*); the downside of this technique is that the image can result distorted, due to the different exposure time of the rows of the same frame (see Figure 3.2).

Therefore, the correct choice of a camera depends on the specific application; if a high number of frame per second (FPS) is needed (e.g., more than 50), as in experiment on studying fast phenomena (e.g. intracellular events), then a CMOS camera would fit well the constrains; if the sample is not fixed, but freely to move, then a CCD camera could be the easier choice. However, it is also possible to find on the market CMOS cameras able to switch among these two reading techniques, making them more attractive due to their flexibility in different applications.

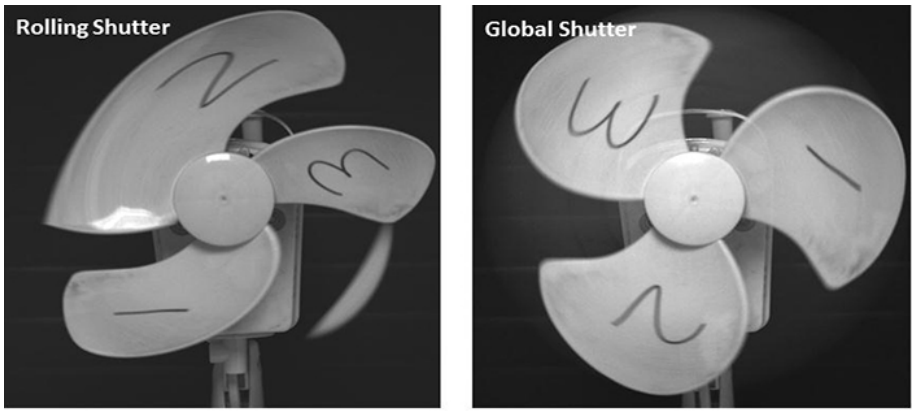

Figure 3.2: Comparison between Rolling and Global Shutter. Because of the different exposure time, rows are read in different moments, leading to an image with bent objects [46].

Both CCD and CMOS cameras can be assessed according many parameters. Here, the most important ones are listed.

QUANTUM EFFICIENCY

The quantum efficiency express the throughput of the camera sensor, in terms of generated photoelectrons. Indeed, not all the photons that hit the camera are converted in electrons: some of them are absorbed by structural material, some miss photodiode and some of them that actually hit the light-sensitive region of the photodiode, fail to emit a photoelectron. This parameter is expressed as a percentage and tells the average number of photons that are able to elicit photoelectrons. This parameter strongly depends on the wavelength and, to a lesser degree, on temperature.

NOISE

In an ideal scenario, each pixel is represented by a certain amount of photoelectrons that are converted in a grey value. Unfortunately, there are some sources of noise that introduce an uncertainty in the intensity value, decreasing the signal-to-noise ratio (SNR). SNR is defined as the ratio of photoelectrons to the sum of all the four sources of noise, measured in electrons.

The first one is due to the *Poisson noise*. It is impossible to completely eliminate, but it can be reduced by increasing the exposure time (i.e. increasing the number of the collected photons). Indeed, it is related to the stochastic distribution (i.e. Poisson distribution) of the arrival of photons at the camera chip. In fact, it is possible to estimate only an average number of photons that a given source of light is able to send towards the camera sensor, each second. It means that this number changes in time, following the Poisson distribution, in which the standard deviation is equal to the square root of the measured number of photons.

The second one is called *Read Noise* and it is the dominant source of noise. It is due to

the imprecision of the read amplifier while measuring the amount of photoelectrons. As for the Poisson noise, it can be only lowered, again by increasing the number of collected photons. Moreover, the read noise is highly affected by the readout speed, since a faster reading of the photoelectrons leads to a less precise measurement. In CCD cameras it is often expressed in root mean square, whereas CMOS datasheets report it as median pixel read noise value.

The third one is the *Dark Current* noise. It is also called $Thermal\ Noise$, since it is due to the temperature of the chip. Indeed, when a camera is working, there is a certain amount of energy that is converted into heat that induces a release of electrons in the chip. For this reason, it is possible to find cooling systems that chill the camera chip, in order to minimize this noise; it is measured as $\frac{e^- \cdot sec}{pixel}$.

The last source of noise is called $Fixed-PatternNoise$ and it is related to the different behaviour of each photodiode. In fact, it is nearly impossible to have same efficiency for each photodiode contained into the camera sensor, meaning that some of them collect and hold photoelectrons in different ways than other, leading to a sensitivity of the sensor that changes spatially. This effect turns to be more evident when the exposure time increases. The fixed-pattern noise can be also unrelated to the detector, since it can arise from dust particles stuck on the camera. CMOS cameras are more affected by this kind of noise than CCD, since it can be related also to variations in the gain of different amplifiers. Often, this noise is after acquisition, thanks to several correction methods.

SNR - DYNAMIC RANGE

In order to evaluate the camera performances, these two parameters must be taken into account. The difference between them is that while SNR includes all the sources of noise, the dynamic range takes into account the read noise only; both of them are usually measured in dB.

ABSOLUTE SENSITIVITY THRESHOLD

This parameter is useful to understand what is the minimum number of photons that have to hit the chip, until that the signal reaches the same intensity level of the noise.

SATURATION CAPACITY

It indicates the number of photoelectrodes that can be stored before the end of the frame exposure. IF more photons hit a saturated photodiode, no more photoelectrodes will be stored inside; its unit is e^-.

BIT DEPTH

It refers to the number of bits of ADCs and, hence, determines the number of the different possible grey levels for each pixel, between 0 (black) and 1(white). Usually, modern cameras have from 10 to 14 bits, since it is demonstrated that over a certain threshold, higher bit depth no longer introduce information.

Other than these parameters, there is also the **Frame Rate**, expressed in FPS, which is the number of frame captured in one second; **Resolution**, which is the dimension, in pixel, of the camera sensor and the **Pixel Size**, which tells the dimension, in μm, of each pixel.

As it is easy to imagine, the perfect camera does not exists, or at least, the one that is the closest to the perfection is very expensive (i.e. from ten to twenty thousands of dollars). Hence, according to the specific experiment and sample, one can make trade-offs between all the parameters and eventually choose the camera that fits better the constraints.

In 1P calcium microscopy, the parameters to take seriously into account are: high quantum efficiency at the specific emitted wavelength, low read and dark current noise (when the fluorescent signal is very weak), medium FPS (it depends on how fast is the neuronal activity that must be recorded) and good resolution, in order to distinguish two different contiguous neurons.

3.5 Setup

In this section, the developed customized 1P setup is described, providing information about the chosen components and the possible operating modes.

As already stated in this chapter, the choice of the components are strictly related to the experiment that has to be performed. In this case, GCaMP6s C. elegans, as well as GFP fixed mouse brain slices have been used. Therefore, as already shown in Figure 1.3 the setup must be calibrated for that green fluorophores, i.e. absorption peak at 488 nm and emission peak at 510 nm. Furthermore, the temporal dynamics of calcium activity determines the required FPS of the camera; C. elegans are characterised by having slow neuronal activities, from few to tens of seconds [47][48][49]. Hence, the required camera needs to work with a minimum frame rate of 5 FPS. Lastly, the size of the neurons affects the magnification factor of the objective. Mice brain cells have an average diameter of around 20 nm, whereas the C. elegans cells are about one order of magnitude smaller, ranging from 1 to 2 nm [50][51]. Therefore, for the GFP slices, an 8x magnification objective is sufficient, whereas for the transgenic worms, the setup needs at least a 25x objective. The small size of the worms defines other limits for the camera parameters, such as resolution and SNR. In fact, in order to sense intensity variations coming from small sources (i.e. neurons), it is necessary to reduce as much as possible the noise and to work with a resolution of at least 1 Megapixel.

Figures 3.3-3.4 show the sketch and a picture of the setup, respectively; the used components are the following:

LIGHT SOURCE

A 50 mW, 473 nm OEM DPSS laser from *Ultralaser* is employed to illuminate and excite fluorophores contained in the samples. The related absorption intensity at that

wavelength is still high enough (around 80%, recall Figure 1.3) to guarantee a good level of fluorescence. Furthermore, in this way no excitation filter is needed.

EMISSION FILTER

The *Thorlabs MF525-39* emission filter. Even if its centre wavelength is 525 nm, the transmission factor at 510 nm is 94.4%, therefore the detector (i.e. the camera) is able to receive almost all the emitted light (again, recall Figure 1.3).

OBJECTIVE LENS

In order to capture detailed pictures of many fluorescent neurons at the time in GFP mouse brain slices, the *BAUSCH & LOMB* LWD $8x$ objective lens, with 0.15 NA and a working distance of 2 cm has been used; when working with C. elegans, due to their small feature, a $25x$/0.31 NA has been utilized (WD 1.3 cm).

CAMERA

FLIR Point Grey BFS-U3-51S5C-C CMOS camera. It has a high resolution (2488 x 2048), with a pixel size of 3.45 μm x 3.45 μm and a frame rate of 75 FPS; the green quantum efficiency at 525 nm is 66% and the read noise is 2.38 electrons.

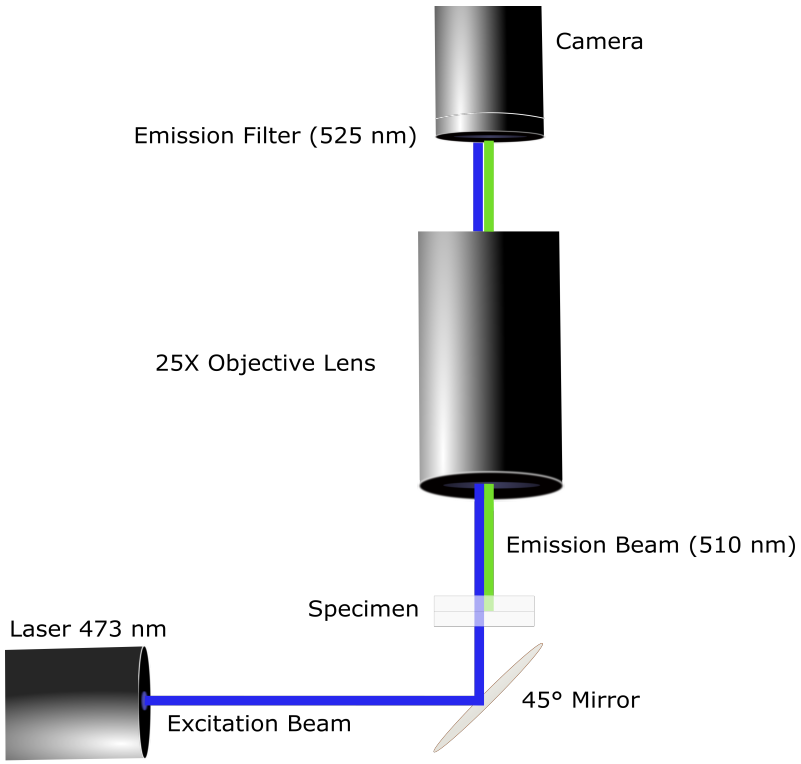

Figure 3.3: Drawing of the schematic of the designed setup.

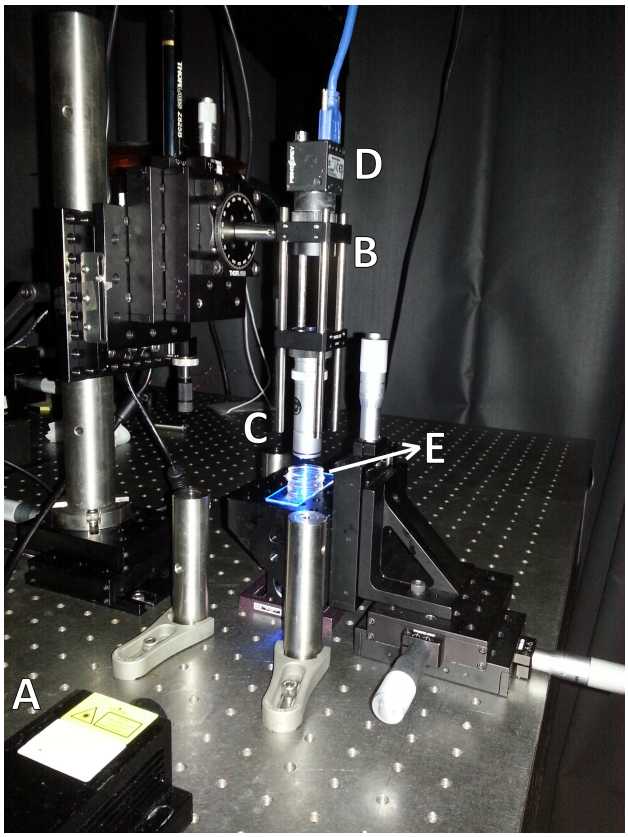

Figure 3.4: Picture of the setup assembled in the laboratory. It is possible to recognize the laser (A), the emission filter (B), the objective lens (C), the camera (D) and the sample (E).

The above shown setup is configured for performing experiments in transmission mode. It means that the emitted light follows the same direction of the excitation laser beam. If needed, this setup can be switched to operate in reflection mode. Conversely to the previous case, when the experiment is performed in reflection mode, the emitted light propagates along the opposite direction of the laser beam, as shown in Figure 3.5.

Of course, when switching from transmission to reflection mode (and vice-versa), the setup has to be changed slightly. In fact, as it is possible to see from Figure 3.5, this time the laser beam passes through the objective lens toward the sample. Therefore, another component is needed and it is called dichroic filter. Such a filter is able to behave differently, according to the wavelength of the beam that impinges on its surface. It is characterised by having a reflection and transmission band, so that it can be almost transparent for a certain band of wavelengths and, on the same time, an almost perfect mirror for others.

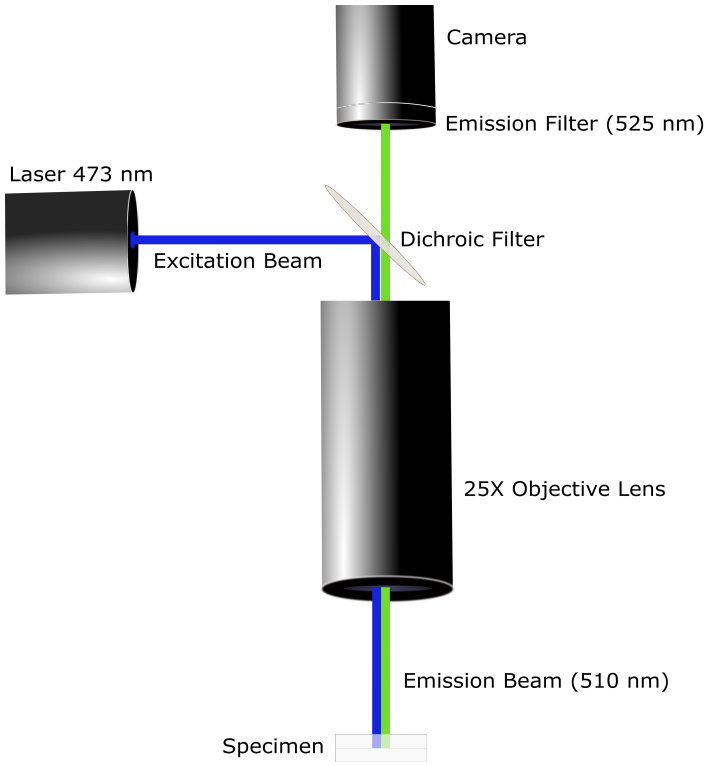

Figure 3.5: Schematic of the designed setup in reflection mode.

Therefore, in reflection mode, the following component has to be added to the previous list:

DICHROIC FILTER

Thorlabs MD498. Its reflection band is 452 - 490 nm, whilst the transmission band is 505 - 800 nm which make this component well suited for the purpose. Indeed, almost all the incoming light is reflected toward the animals (its transmittance at 473 nm is only 3.1%) and, in the same time, almost all the emitted light is transmitted toward the emission filter (its transmittance at 510 nm is 94.3%).

When switching from transmission to reflection mode, one has to consider that, since the illumination path goes through the objective lens, the beam size on the sample will be reduced by a factor that depends on the magnification of the objective. Therefore, the intensity of the light on the specimen will increase by the same factor.

As stated in the Introduction, the assembled setup is fully compatible with the already presented acousto-optic technology, since there is enough space for integrating the cylindrical piezoelectric transducer, as shown in the picture depicted in Figure 3.6.

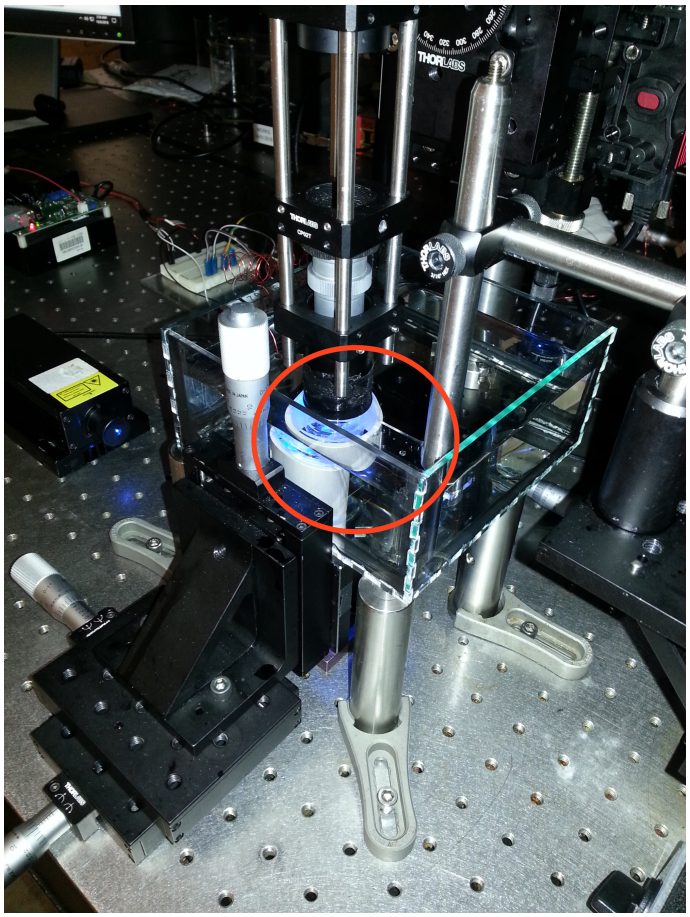

Figure 3.6: Picture of the setup when employing the acousto-optic technique. In the red circle: the transducer, the dropdown fixture with the sample and a tube with a glass window in order to avoid putting the objective in contact to the water (it is not waterproof).

The piezo-transducer is immersed into a container filled with a 2% Triton X-100 solution in deionized (DI) water, in order to avoid both cavitation and electricity inside the cavity of the transducer; the sample is placed inside the cavity and held by a dropdown fixture that can adjust the positioning of the specimen along x,y and z directions. Since the objective lens is not waterproof, a tube with a glass window is used so that it can be immersed inside the liquid medium. Thanks to its long working distance (1.3 cm), it is possible to focus on the sample, being outside of the cylindrical cavity (otherwise it would affect the ultrasound pattern inside the transducer).

Chapter 4

Imaging Tissue Phantom

In this chapter, a brief description of the employed transgenic worms is provided, as well as the procedure to prepare the living brain tissue phantoms used to test the developed 1P setup.

Performing experiments on living animals is a necessary step when researching for human diseases. Indeed, it is very useful to study the mechanisms that govern a specific behaviour, or to assess the effect of a specific drug, for instance. However, not all the existing animals are suitable for this kind of analysis, since many of them do not share biological properties with the human race. For this reason, it is possible to find in literature a list of model animals, from very simple organism, to evolute and complex animals with genome very similar to the one of human beings.

The main problem with working with animals is that it is not ethically correct to use them if there is no an evident, or ensured benefit from their exploitation. For this reason, especially during the very first stages of a study, it is always recommended employing samples that can reproduce at least some properties of a tissue so that it can be used as a proof of concept demonstration of the specific research. This kind of samples are called *tissue phantoms*. As a part of goal of this thesis, a new concept of tissue phantom has been provided, that meets both the requirements of being affordable and ethical. In fact, it is based on living transgenic worms, able to be recovered after the experiment.

4.1 Caenorhabditis elegans

The nematode Caenorhabditis elegans is a very simple, ideal model organism, widely studied worldwide for understanding questions of developmental biology and neurobiology, as in neurodegenerative disorders such as Parkinson disease [52]. One of the most important features that leaded C. elegans to be so popular in research is that its tissue is transparent, hence it allows a very easy living-observation of each cell under a microscope. Furthermore, the birth of calcium imaging and GECIs allowed to perform *in-vivo* experiment and real-time studying of neural mechanisms.

Figures 4.1-4.2 show the neuron mapping in C. elegans; most of the neurons are located

into their head, in a sort of brain, or somatic nervous system, whilst the rest of them belong to the small pharyngeal nervous system. These two nervous systems are distinct and independent and communicate each other through a single pair of interneurons. The total number of neurons in an adult C. elegans changes slightly, according to the gender: 385 in males, 302 in hermaphrodite [53].

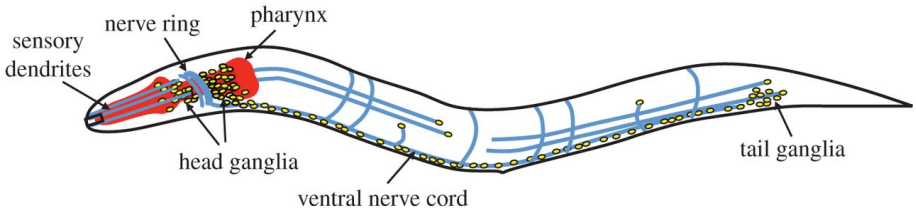

Figure 4.1: Drawing of the two nervous systems in C. elegans [54].

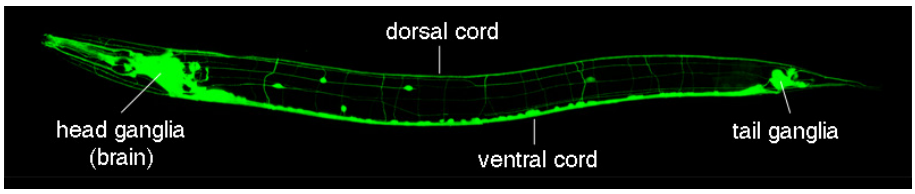

Figure 4.2: GFP marker used to highlight the nervous systems [55].

Freely moving C. elegans are generally characterised by having a slow spontaneous neuronal activity. For this reason, it is possible to stimulate them using a several different techniques. They react to mechanical (e.g., body touch and ultrasounds [56]), chemical (e.g., odorants, tastants and oxygen [57]) and light stimuli [58].

Although they do not have eyes, they are able to respond to light stimulation, when shone with a range of wavelengths that goes from UV-A (350 nm) to yellow (575 nm). Indeed, they show a negative phototaxis behaviour, essential for survival: a prolonged exposure to UV, violet and blue light paralyses and kills the worms; increasing the intensity of the exposition, the necessary time span, after which the animal dies, decreases. This is a critical problem to take into account while working on GCaMP C. elegans, since a blue light is needed in order to excite the fluorophores. Hence, the intensity of the light source has to be adjusted so that the worms survive the experiment; employing a blue light, with an intensity of 20 mW/mm^2 they can stay alive for about 15 minutes [58].

Because of their negative phototaxis behaviour, it is highly recommended to immobilize them before performing calcium imaging experiments, in order to avoid neurons overlapping during the crawling.
There are four standard techniques used to immobilize worms:

- pharmacological paralysation [59], in which anaesthetics like Levamisole and Sodium Azide are used to paralyse worms. The drawback of this technique is that, as a consequence of using anaesthetics, the synaptic transmissions in the animals are highly reduced;

- gluing them by using non-toxic medical adhesive [60]. Even though worms are awake, glue is a highly refractile material and, most of them, have a dye which is fluorescent when viewed under a GFP filter set;
- employ polystyrene microbeads [61]. This technique is a variation of the first one, since instead of pouring small amount of liquid anaesthetic, a microbead (or nanobead) solution is employed so that the friction between substrate, worms and cover glass is increased so highly, that they are not able to move.
- use microfluidic devices [62], that can be designed and built according to the specific experiment, in which worms are trapped by thin cavities of the structure. This is the most complex and expensive solution for immobilize worms.

4.2 Living Brain Tissue Phantom

As already stated, tissue phantoms are samples used to test the feasibility and the outcome of a specific application, since they can behave as the real tissue, or medium, on which the research is focused on. The very final goal of this work would be to apply the acousto-optic technology in living human brain, in order to stimulate and record activity in the less invasive way as possible. Of course, before reaching that final stage, the research has to carry out intermediate steps, in order to validate the technique.

A brain tissue can be characterised by electrical, mechanical, chemical and optical properties. Since the acousto-optic technique exploits standing wave pressure to confine light into a medium, in order to verify the reliability of such a technology, it is necessary to replicate a sample that behaves mechanically and optically as a brain tissue does. For this reason, agarose has been used to make the tissue phantoms. In fact, this material, when mixed with water and solidified, is in a gelatine form; with low weight/volume concentrations, agarose gels accurately emulate the poroelasticity of the brain [63][64]. For what concern the optical properties, still, agarose powders can be mixed with another liquid solution (i.e. *Intralipid* 20%) together with water, in order to decrease the transparency and get a final medium optically comparable to the brain tissue, in terms of scattering (not done during this thesis) [41].

The presented living brain tissue phantom combines the mechanical and optical properties carried by the agarose gel, with the presence of living immobilized transgenic C. elegans worms. Such a sample can be used for several applications in electro-physiology and optogenetics.

The preparation of the sample consists of few steps: prepare two agarose layers, place worms onto one of them and finally cover worms applying the other agarose layer, sealing the sample. Since the worms are able to crawl inside this sort of agarose sandwich, the chosen immobilization technique is the one that employs the microbeads solution.

4.2.1 Preparation of 2% Agarose

The powdered agarose is first mixed in DI water at room temperature in a Pyrex beaker, covered by an aluminium foil to prevent evaporation. A concentration of 0.8 g

agarose in 100 *ml* of deionized water is used. Then the solution is constantly mixed with a magnetic stirrer at 600 *rpm*, while the temperature is increased to the boiling temperature of the solution. When the solution is boiling, the hotplate is turned off and the temperature of the mixture monitored. After 5 minutes, the solution is poured into a rectangular mould to form a rectangular phantom. The bottom of the moulder is sealed with a smooth non-stick glass plate to ensure the facet of cast phantom is smooth. As the solution reaches room temperature, move it to a refrigerator, where it is kept at 6°C for 30 minutes. Prolonged exposure to air causes the moulded phantom to shrink in size and become opaque. To prevent the shrinkage, keep agarose gel phantoms in deionized water after fully cured.

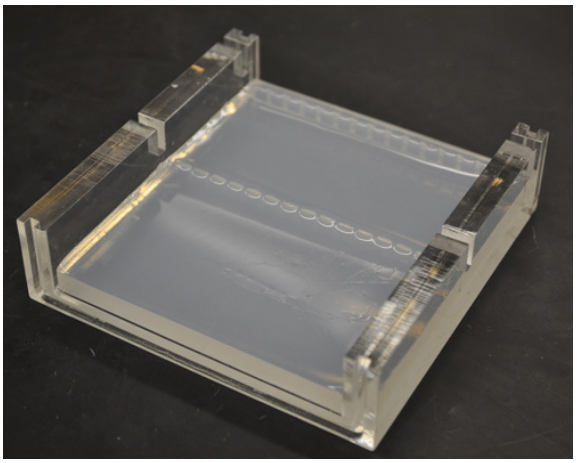

Figure 4.3: Two 2% agarose samples obtained using a rectangular moulder.

4.2.2 Mounting of Worms

Under a stereo microscope, transfer tens of worms to a clean petri dish, seeded with Nematode Growth Medium (*NGM*) and leave the plate for around 1 minute. During this time, the worms will crawl freely onto the clean surface, leading to a self-removing of bacteria from the worms skin. In the meantime, pour 1 μL droplet of of 2.6% 100 *nm* diameter polystyrene microbeads in water, onto one gelified layer of agarose. Then, transfer around ten animals from the clean NGM petri dish to the microbeads solution. To ensure that they do not overlap each other, use the worm picker to spread them inside the liquid. Afterwards, apply the other agarose layer, pushing gently to remove air bubbles, without crushing C. elegans. The phantom tissue is now ready for imaging.

Both optical and mechanical properties, can be easily customized according to the needs by either increasing or decreasing the agarose concentration. However, whether increasing the concentration results in a more scattering phantom tissue, it turns to be stiffer, loosing the typical poroelasticity of brain tissues. To overcome to this issue, it is possible to add scattering solutions (e.g., *Intralipid* 20%) when preparing agarose layers.

Chapter 5

Conclusions

Here, to demonstrate the reliability of the developed 1P microscope, several pictures are shown. In detail, the specimens employed to test the setup are GFP fixed mouse brain slices and the already presented living brain tissue phantom. Last, a discussion about the obtained results and future works.

5.1 Results

5.1.1 GFP Mouse Brain Slices

The very first experiment has been carried out on GFP fixed mouse brain slices, in reflection mode. The pictures shown in Figure 5.1 are depicting two random regions of two different slices; both of them have been taken by employing the setup shown in Figure 5.2.

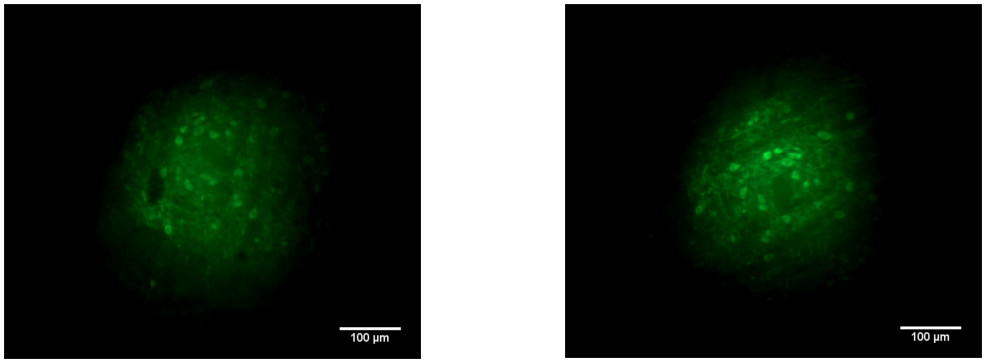

(a) GFP slice 1 (b) GFP slice 2

Figure 5.1: Fluorescent mouse brain tissue. It is possible to clearly distinguish many neurons and axons. The different intensity of emitted light is not due to different camera settings, but because of photobleaching.

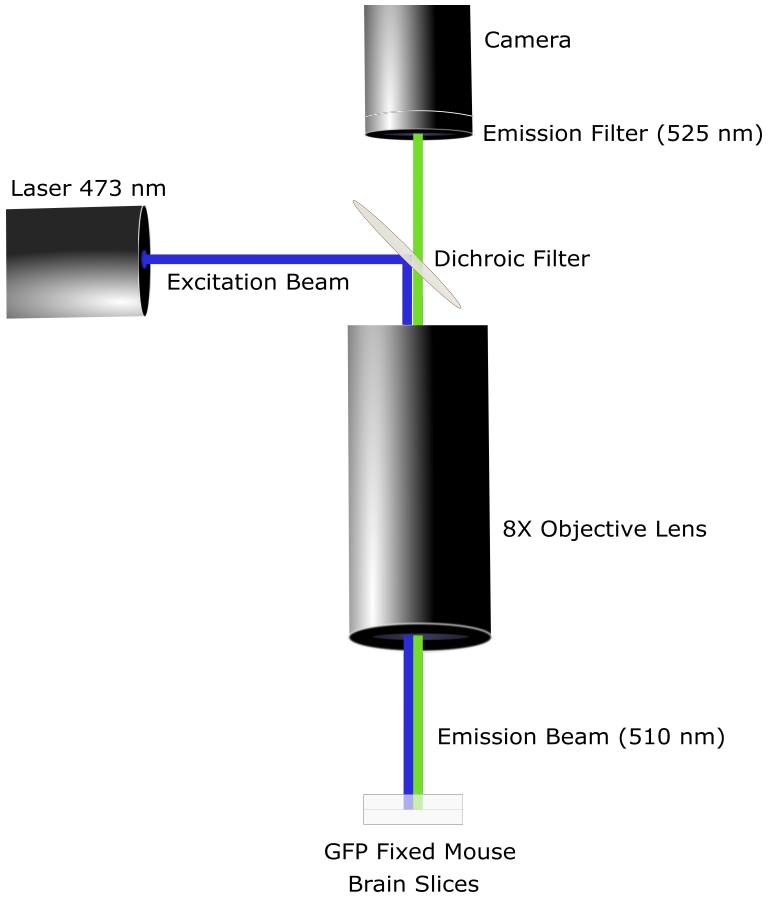

Figure 5.2: Schematic of the utilized setup.

Here, are reported the camera and laser settings:

- CAMERA
  - Exposure Time: 28 ms;
  - Gain: 0.
- LASER
  - Operating Mode: Continuous Wave;
  - Voltage: 3 V.

With the above settings, the intensity of light on the surface of the sample is 108 mW/mm^2.

5.1.2 C. Elegans

Multiple experiments have been carried out on C. elegans: in the first stage, they have been used in order to test the feasibility and reliability of the living brain tissue phantom (Section 4.2). For this reason, many videos about neuronal activity have been recorded.

Lastly, they have been also used as a target of the virtual optical waveguide, sculpted inside the phantom tissue thanks to the use of the acousto-optic technology (Section 2.3).

CALCIUM IMAGING

Once prepared a 6 mm thick living brain tissue phantom (as explained in Section 4.2), the sample has been positioned under the 1P microscope setup in order to perform calcium imaging. Conversely to what done for the previous experiment on mouse slices, now a $25x$ objective lens is necessary, in order to capture the smaller C. elegans neurons (around 2-5 nm). The schematic of the employed setup is not showed, since it is exactly the same already depicted previously in Figure 5.2, except for the magnification factor of the objective lens.

The reflection mode was preferred with respect to the transmission one, since the laser beam is more concentrated due to the fact that it passes through the objective. This feature gives an advantage in terms of contrast: as the beam spot increases in size, the intensity on the sample decreases and, above all, the excited area increases. Therefore, the background light is enhanced, making less evident the contrast between the target and the rest of the sample.

Many videos showing calcium activity have been recorded. Thanks to the presence of the GCaMP6s, it is possible to see variations of the emitted fluorescent light intensity over the observation period. Two frames have been extracted from one video, showing two neurons firing over time (Figures 5.3a-5.3b). Afterwards, to assess the temporal dynamics of the neuronal activity, $\Delta F/F$ graphs have been plotted (Figures 5.4a-5.4b). Each of them represents the variation of the fluorescence emission (ΔF) over the baseline level of fluorescence (F).

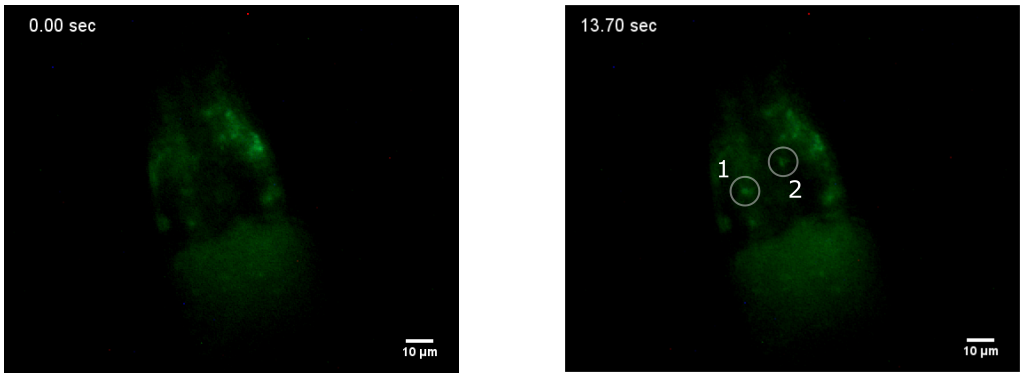

(a) (b)

Figure 5.3: Pictures show fluorescence change in two neurons before (a) and during (b) neuron activity.

Camera and laser settings:

- CAMERA
  - Exposure Time: 100 ms;

  - Gain: 27.7.

- LASER

  - Operating Mode: Continuous Wave;
  - Voltage: 2 V.

To reduce the intensity of the light on the sample, an absorptive neutral density filter 2.0 (NE20A-A, from *Thorlabs*) has been used; the transmitted light across the filter, at 473 nm, is 0.9%, and it gives an intensity of 18 mW/mm^2 on the sample, which is slightly less than the intensity level that allows experiments on worms for 15 minutes, before their death [58].

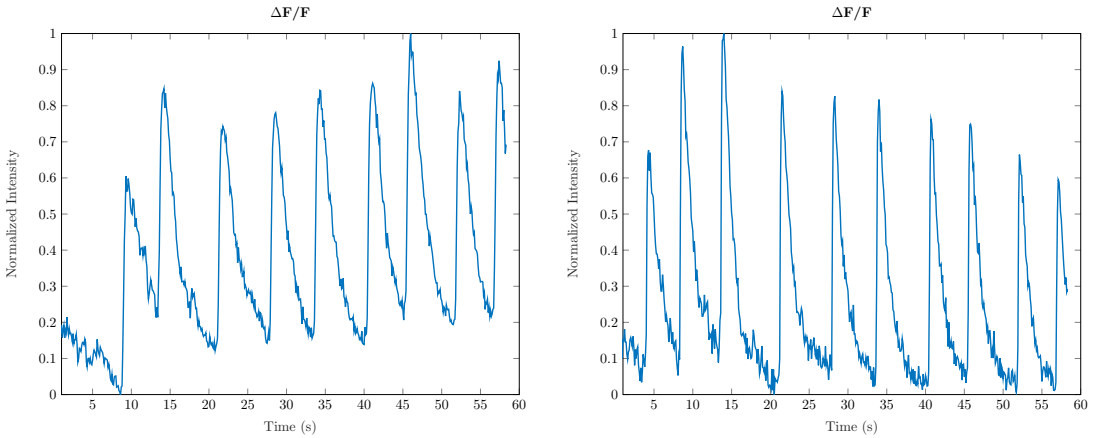

(a) Neuron 1 (b) Neuron 2

Figure 5.4: $\Delta F/F$ graphs of the two neurons highlighted in Figure 5.3b.

VIRTUAL OPTICAL WAVEGUIDE

As a third step of this thesis work, the living brain tissue phantom has been employed as a proof of concept demonstration of the already mentioned virtual optical waveguide (Section 2.3). The goal of this experiment was to demonstrate that, with this novel technique, it is possible to selectively stimulate with light a specific region of the targeted tissue. For this purpose, the piezoelectric cylindrical transducer has been integrated in the setup, which worked in transmission mode, conversely to what done for the previous experiments. In this way, it is easier to assess the effect of ultrasound on the beam spot.

The schematic of the used setup is reported in Figure 5.5 (picture in Figure 3.6).

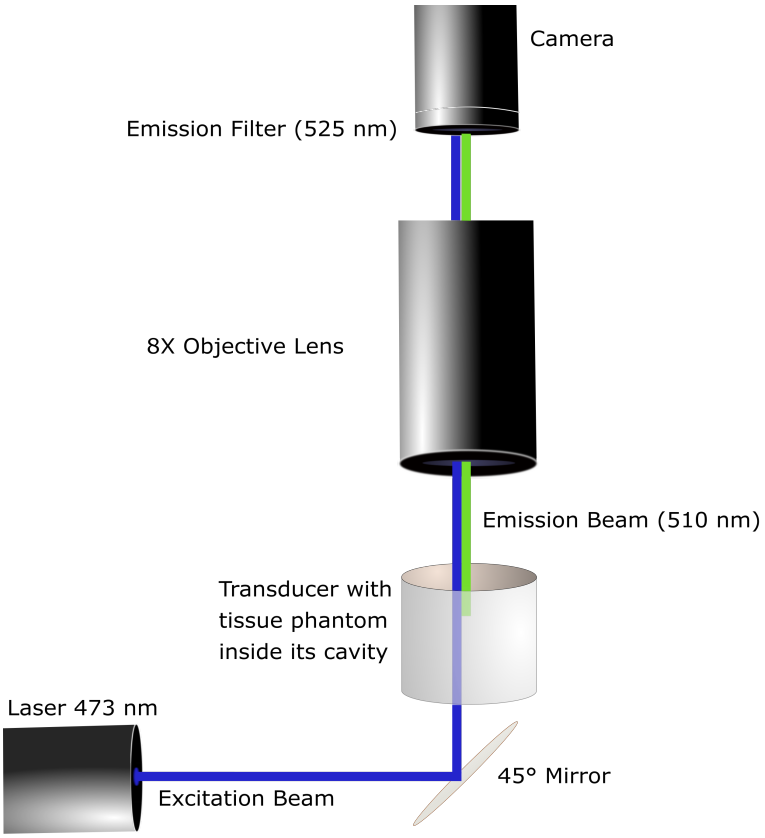

Figure 5.5: Schematic of the utilized setup. The transducer is immersed in a container filled with 2% Triton X-100 solution in DI water. Triton is needed to avoid cavitation; even though the transducer is insulated electrically by a thin layer of Parylene, imperfections on its surface could lead to current leakage, hence the DI water is used to prevent it.

Before performing the experiment on C.elegans, the virtual optical waveguide has been tested in water (2% Triton X-100 solution in DI water). Results are shown in Figure 5.6.
Transducer and laser settings:

- TRANSDUCER
  - Input Signal: Sine Wave;
  - Resonance Frequency: 833 kHz;
  - Voltage: 0-10 V.
- LASER
  - Operating Mode: Continuous Wave;
  - Voltage: 3 V.

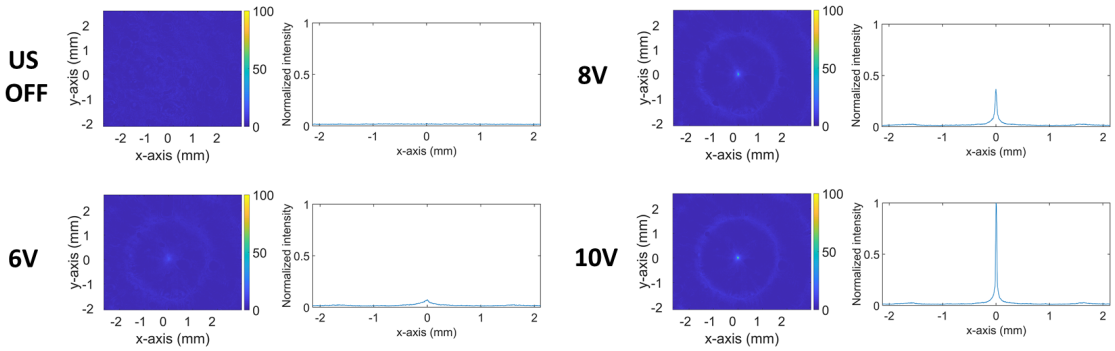

Figure 5.6: As explained in Section 2.3, the transducer is able to sculpt a virtual optical waveguide inside its cavity, due to a refractive index modulation of the medium; the higher the input voltage, the higher the modulation, hence the more efficient the virtual optical waveguide. The pictures are in false colour, in order to highlight the effect.

As expected from the theory, the bigger refractive index contrast, that leads to a more confinement of the light, is obtained in the centre of the transducer cavity. Indeed, here, the medium reaches its maximum level of compression, due to the standing pressure waves launched from the walls; changing the voltage, the efficiency of the virtual optical waveguide changes accordingly.

The living brain tissue phantom is held inside the cavity by a dropdown fixture, so that the worms are placed on the top surface of the transducer. Results of the effect of ultrasound are shown in Figure 5.7. In order to have a larger field of view, the $25x$ objective has been substituted by the $8x$ one.

Camera and laser settings:

- CAMERA
  - Exposure Time: 100 ms;
  - Gain: 28.8.
- LASER
  - Operating Mode: Continuous Wave;
  - Voltage: 1.8 V.

As already done for calcium imaging, an absorptive neutral density was necessary to reduce the intensity of light. This time a 0.2 filter has been used (NE02A-A, from *Thorlabs*) to reduce the transmitted light by 26.9%, at 473 nm (different filter, since this time the setup was in transmission mode, hence the beam spot was larger than before). With this configuration, the intensity on the sample is 35 mW/mm^2.

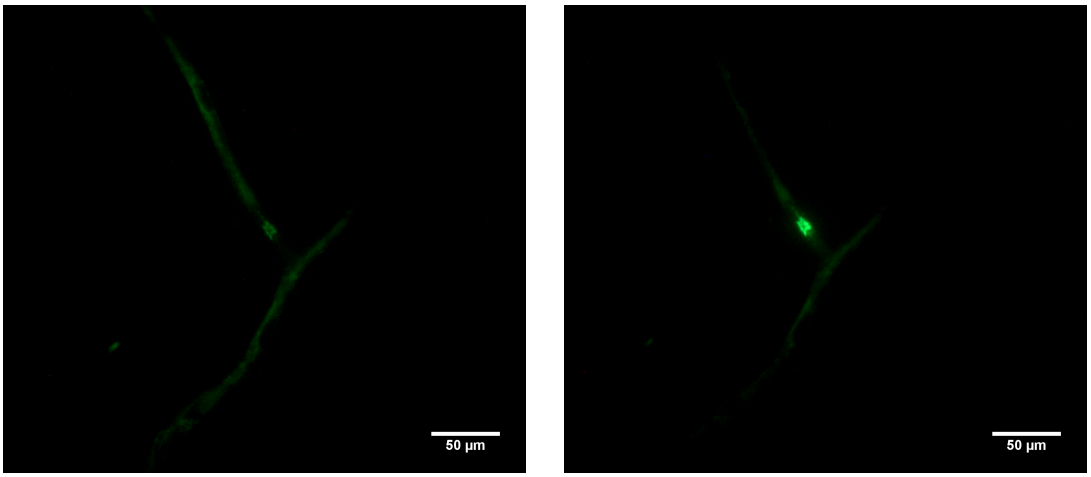

(a) Ultrasound OFF (b) Ultrasound ON

Figure 5.7: The virtual optical waveguide is sculpted inside the living brain tissue phantom. The scattered light on the background is recollected and confined around the centre of the image (i.e. into the virtual optical waveguide), leading to an increase in intensity of the fluorescence emitted by neurons.

5.1.3 Virtual Relay Lens

To investigate the features and the reliability of the transducer as a virtual relay lens, a couple of experiments have been carried out, without using neither C. elegans, nor GFP mouse brain slices. Indeed, the sample imaged was a tissue phantom obtained mixing agar and green fluorescein, which is an organic compound able to behave as a standard GFP. In order to define features to image on the sample, a negative mask has been placed on top of the tissue phantom, as depicted in Figure 5.8. Thus, the experiment consisted in relaying the fluorescent image (i.e. CMU) placed on the bottom of the transducer, while the camera was focusing its top edge. In Figure 5.9 the results.

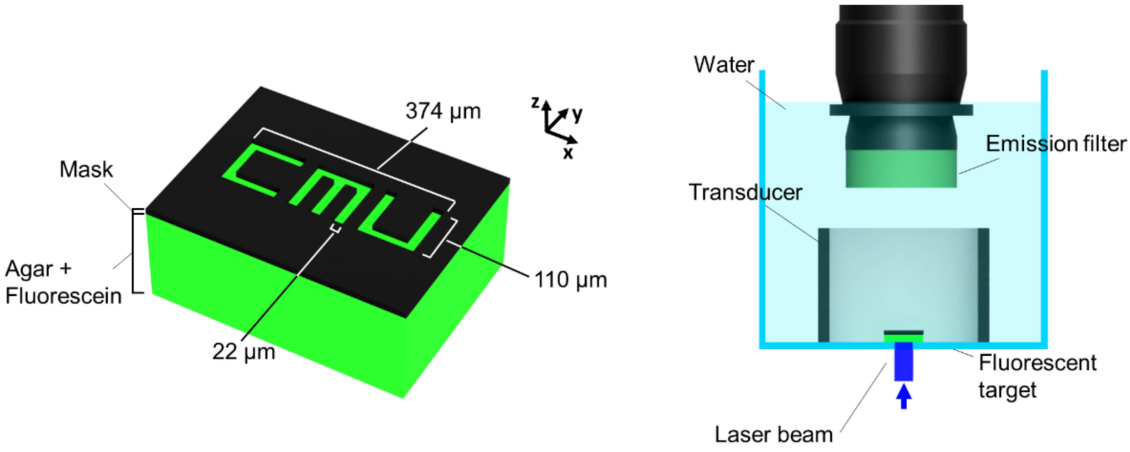

Figure 5.8: Detail of the mask (left) and a schematic of the used setup (right); the target is 30 mm behind the camera focal plane (which is at the top surface of the transducer); the employed objective lens has a magnification factor of 2.25x.

Camera, laser and transducer settings:

- CAMERA
  - Exposure Time: 2.8 ms;
  - Gain: 0.
- LASER
  - Operating Mode: Continuous Wave;
  - Voltage: 3 V.
- TRANSDUCER
  - Input Signal: Sine Wave;
  - Resonance Frequency: 833 kHz;
  - Voltage: 0-50 V.

Lastly, the experiment has been repeated again, changing the optical properties of the medium, adding 1.25 mL of *Intralipid* 20% in 1 L of 2% of Triton 100-X in DI water. The OT of the obtained scattering medium is 5.9 MFP. In Figure 5.10 it is possible to qualitatively understand the scattering level of such a medium, whereas in Figure 5.11 the results are reported.

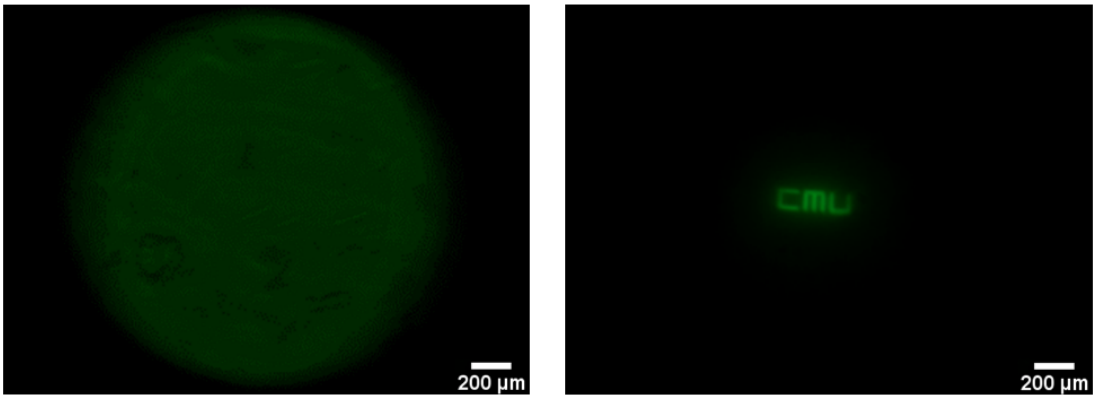

(a) Ultrasound OFF (b) Ultrasound ON

Figure 5.9: When ultrasound is off, the camera sees only a blurred image, since the target is far from its focal plane; with ultrasound on, the virtual relay lens is active and the sample turns to be in focus.

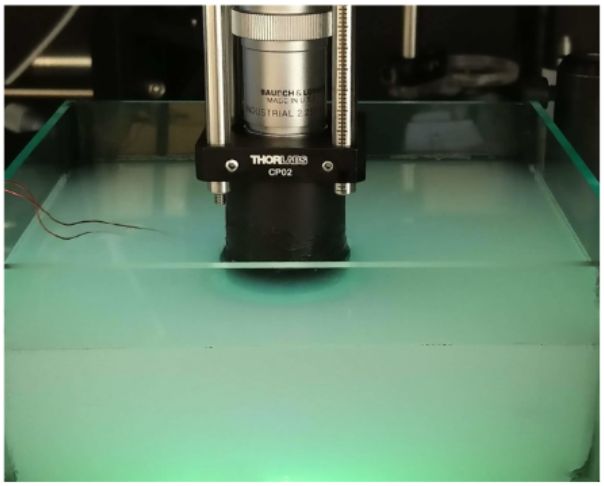

Figure 5.10: Picture of the employed medium.

5.2 Discussion

The goal of the presented thesis was to develop a customised one-photon calcium imaging setup, able to combine traditional imaging techniques and an innovative acousto-optic stimulation. Furthermore, it has been also presented a new concept of living brain tissue phantom, based on GCaMP6s C. elegans worms.

After a period spent designing the microscope, its reliability has been tested through several experiments and adjustments.

Testing the setup consisted in:

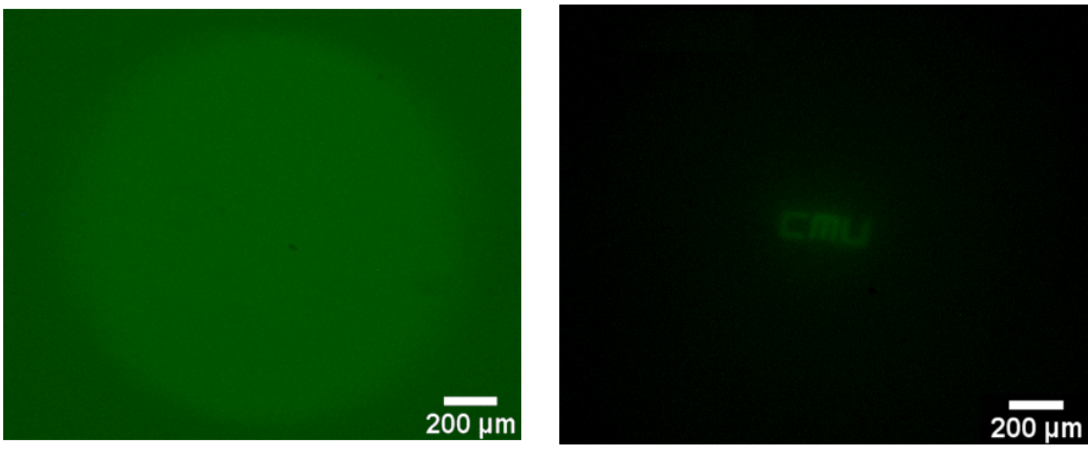

(a) Ultrasound OFF

(b) Ultrasound ON

Figure 5.11: The transducer is able to relay the image in a 5.9 MFP scattering medium; the exposure time used for (a) is 3 times higher than the one used for (b).

- performing experiments on GFP fixed mouse brain slices to assess the fluorescence imaging quality;
- repeating the experiment exchanging the brain slices with living GCaMP6s C. elegans, to evaluate fluorescence and temporal dynamics.

Afterwards, the following experiments have been carried out:

- characterisation of a protocol for building the tissue phantom;
- calcium imaging in C. elegans (inside and outside the living brain tissue phantom);
- application of the virtual optical waveguide during stimulation of neurons;
- investigation about the virtual relay lens.

The obtained results showed that the presented setup is able to perform imaging and calcium imaging in GCaMP6s C. elegans, with the advantage of an easy adaptation to many application, by interchanging its operation between reflection and transmission mode. Moreover, each component can be easily removed for future improvements. When combined with the acousto-optic technology, the potentiality of this microscope enhances, allowing non-invasive stimulations of specific single neurons thanks to the virtual optical waveguide. In fact, the piezoelectric cylindrical transducer makes possible the steering of light inside a scattering medium, reaching depth of penetration unachievable to standard 1P microscopes.

Regarding the living brain tissue phantom, results showed the feasibility of performing calcium imaging experiments on it. The preparation of such samples is very easy and cost-effective, that make them affordable for any laboratory and any purpose, without the needs of surgery skills, animal facilities and certifications. Optical and mechanical

properties can also be easily tuned by changing the concentration (or even the materials) of the solution, making them adaptable to many different applications.

The virtual relay lens effect has been observed positively in relaying images in both transparent and turbid media (OT of 5.9 MFP), suggesting that this phenomenon could be very useful to increase the achievable imaging distance through a tissue, or a scattering medium in general, without employing invasive solutions (e.g., implantable probes and waveguides).

5.2.1 Future Works

In the very first next step, the developed setup should be used to perform the virtual relay lens experiment on C. elegans; if not working with worms because of their too weak fluorescent signal, then a good solution could be to switch to bigger fluorescent animals, like *Hydra* polyps. A stronger signal would facilitate calcium imaging as well, decreasing the noise level introduced by the high camera gain, needed to observe neuronal activities. Besides, bigger animal would mean bigger neurons, hence easier imaging.

In terms of components, without mentioning trivial suggestions (e.g., buying a camera with higher performances, or an objective with higher numerical aperture), it has to be mentioned the importance of a new laser capable of being modulated at high frequencies (or, at least, at the same resonance frequencies used for driving the transducer). This change would highly improve the behaviour of the virtual optical waveguide. Indeed, if it were possible to synchronise the laser beam with the pressure profile within the transducer cavity, the virtual optical waveguide could confine much more light than now. This is due to the fact that standing pressure waves generate pressure peaks and troughs along the medium, fixed in space, but their values are varying in time: after half of a period, a peak turns to be a trough and vice-versa. Hence, when using a CW laser, the result is an averaging effect of the laser intensity over time. On the contrary, when a laser is in sync with the pressure medium pattern, it is pulsed in the correspondence of peaks (or troughs) only; it would lead to a perfect coupling between light and pressure, i.e. a highest efficiency of the virtual optical waveguide in terms of confining light (hence, penetration depth).

Bibliography

[1] V. Thakore, P. Molnar, and J. J. Hickman, "An optimization-based study of equivalent circuit models for representing recordings at the neuron–electrode interface," *IEEE Transactions on Biomedical Engineering*, vol. 59, no. 8, pp. 2338–2347, 2012.

[2] A. Donate and R. Heller, "Assessment of delivery parameters with the multielectrode array for development of a dna vaccine against bacillus anthracis," *Bioelectrochemistry*, vol. 94, pp. 1–6, 2013.

[3] R. A. Normann, E. M. Maynard, P. J. Rousche, and D. J. Warren, "A neural interface for a cortical vision prosthesis," *Vision research*, vol. 39, no. 15, pp. 2577–2587, 1999.

[4] U. Egert and H. Hämmerle, "Application of the microelectrode-array (mea) technology in pharmaceutical drug research," *Sensoren im Fokus neuer Anwendungen*, pp. 51–4, 2002.

[5] M. E. Spira and A. Hai, "Multi-electrode array technologies for neuroscience and cardiology," *Nature nanotechnology*, vol. 8, no. 2, p. 83, 2013.

[6] P. Mahmoudi, H. Veladi, and F. G. Pakdel, "Optogenetics, tools and applications in neurobiology," *Journal of medical signals and sensors*, vol. 7, no. 2, p. 71, 2017.

[7] V. Emiliani, A. E. Cohen, K. Deisseroth, and M. Häusser, "All-optical interrogation of neural circuits," *Journal of Neuroscience*, vol. 35, no. 41, pp. 13917–13926, 2015.

[8] K. Zalocusky and K. Deisseroth, "Optogenetics in the behaving rat: integration of diverse new technologies in a vital animal model," *Optogenetics*, vol. 1, pp. 1–17, 2013.

[9] T.-W. Chen, T. J. Wardill, Y. Sun, S. R. Pulver, S. L. Renninger, A. Baohan, E. R. Schreiter, R. A. Kerr, M. B. Orger, V. Jayaraman, *et al.*, "Ultrasensitive fluorescent proteins for imaging neuronal activity," *Nature*, vol. 499, no. 7458, p. 295, 2013.

[10] S. H. Chung, L. Sun, and C. V. Gabel, "In vivo neuronal calcium imaging in c. elegans," *Journal of visualized experiments: JoVE*, no. 74, 2013.

[11] L. Fenno, O. Yizhar, and K. Deisseroth, "The development and application of optogenetics," *Annual review of neuroscience*, vol. 34, 2011.

[12] T. F. Marton and V. S. Sohal, "Of mice, men, and microbial opsins: how optogenetics can help hone mouse models of mental illness," *Biological psychiatry*, vol. 79, no. 1, pp. 47–52, 2016.

[13] J. K. Tung, K. Berglund, and R. E. Gross, "Optogenetic approaches for controlling seizure activity," *Brain stimulation*, vol. 9, no. 6, pp. 801–810, 2016.

[14] J. Akerboom, N. Carreras Calderón, L. Tian, S. Wabnig, M. Prigge, J. Tolö, A. Gordus, M. B. Orger, K. E. Severi, J. J. Macklin, *et al.*, "Genetically encoded calcium

indicators for multi-color neural activity imaging and combination with optogenetics," *Frontiers in molecular neuroscience*, vol. 6, p. 2, 2013.

[15] V. P. Koldenkova and T. Nagai, "Genetically encoded ca2+ indicators: properties and evaluation," *Biochimica et Biophysica Acta (BBA)-Molecular Cell Research*, vol. 1833, no. 7, pp. 1787–1797, 2013.

[16] T. Rose, P. M. Goltstein, R. Portugues, and O. Griesbeck, "Putting a finishing touch on gecis," *Frontiers in molecular neuroscience*, vol. 7, p. 88, 2014.

[17] Y. Zhao, S. Araki, J. Wu, T. Teramoto, Y.-F. Chang, M. Nakano, A. S. Abdelfattah, M. Fujiwara, T. Ishihara, T. Nagai, *et al.*, "An expanded palette of genetically encoded ca2+ indicators," *Science*, p. 1208592, 2011.

[18] M. Ohkura, T. Sasaki, J. Sadakari, K. Gengyo-Ando, Y. Kagawa-Nagamura, C. Kobayashi, Y. Ikegaya, and J. Nakai, "Genetically encoded green fluorescent ca2+ indicators with improved detectability for neuronal ca2+ signals," *PloS one*, vol. 7, no. 12, p. e51286, 2012.

[19] S. Fields and M. Johnston, "Whither model organism research?," *Science*, vol. 307, no. 5717, pp. 1885–1886, 2005.

[20] J. M. Slack, *Essential developmental biology*. John Wiley & Sons, 2009.

[21] T. G. Meijer, K. A. Naipal, A. Jager, and D. C. van Gent, "Ex vivo tumor culture systems for functional drug testing and therapy response prediction," *Future science OA*, vol. 3, no. 2, p. FSO190, 2017.

[22] M. E. Dailey, G. S. Marrs, and D. Kurpius, "Maintaining live cells and tissue slices in the imaging setup," *Cold Spring Harbor Protocols*, vol. 2011, no. 4, pp. pdb–top105, 2011.

[23] C. Stosiek, O. Garaschuk, K. Holthoff, and A. Konnerth, "In vivo two-photon calcium imaging of neuronal networks," *Proceedings of the National Academy of Sciences*, vol. 100, no. 12, pp. 7319–7324, 2003.

[24] Herman, L. Frohlich, S. Murphy, and Davidson, "Fluorescence microscopy - basic concepts in fluorescence." `https://micro.magnet.fsu.edu/primer/techniques/fluorescence/fluorescenceintro.html`, 2015.

[25] I. T. Young, Y. Garini, H. R. Dietrich, W. van Oel, and G. L. Lung, "Leds for fluorescence microscopy," in *Three-Dimensional and Multidimensional Microscopy: Image Acquisition and Processing XI*, vol. 5324, pp. 208–216, International Society for Optics and Photonics, 2004.

[26] INSCOPIX, "Two-photon and miniaturized one-photon microscopy - a technology discussion for neural circuit imaging," tech. rep., 2016.

[27] Alluxa, "Using non-linear optical systems for thin-film optical components." `https://www.azooptics.com/Article.aspx?ArticleID=1175`.

[28] F. Piston and Davidson, "Fundamentals and applications in multiphoton excitation microscopy." `http://www.microscopyu.com/articles/fluor-escence/multiphoton/multiphotonintro.html`, 2016.

[29] R. K. Benninger and D. W. Piston, "Two-photon excitation microscopy for the study of living cells and tissues," *Current protocols in cell biology*, vol. 59, no. 1, pp. 4–11, 2013.

[30] M. A. D. McCoy, "Optogenetics relies on multiphoton microscopy." http://www.imaging-git.com/science/light-microscopy/optogenetics-relies-multiphoton-microscopy, 2015.

[31] Wikipedia contributors, "Piezoelectric sensor — Wikipedia, the free encyclopedia." https://en.wikipedia.org/w/index.php?title=Piezoelectric_sensor&oldid=861368784, 2018. [Online; accessed 29-September-2018].

[32] PI Motion | Positioning, "Displacement modes of piezoelectric actuators." https://www.physikinstrumente.com/en/technology/piezo-technology/properties-piezo-actuators/displacement-modes/. [Online].

[33] M. V. Ravinder S. Dahiya, *Robotic Tactile Sensing*. 2013.

[34] J. Erhart, P. Pulpan, and M. Pustka, *Piezoelectric Ceramic Resonators*. Topics in Mining, Metallurgy and Materials Engineering, Springer International Publishing, 2016.

[35] E. McLeod, *Bessel Beams in Tunable Acoustic Gradient Index Lenses and Optical Trap Assisted Nanolithography*. PhD thesis, Princeton University, June 2009.

[36] E. Murimi, S. Mutuli, G. Nyakoe, and J. Kihiu, "Determination of resonant frequency of a piezoelectric ring for generation of ultrasonic waves," 2011.

[37] N. Adelman, Y. Stavsky, and E. Segal, "Axisymmetric vibrations of radially polarized piezoelectric ceramic cylinders," *Journal of Sound and Vibration*, vol. 38, no. 2, pp. 245–254, 1975.

[38] D. H. Chambers, "Acoustically driven vibrations in cylindrical structures," October 2013.

[39] I. Grulkowski, D. Jankowski, and P. Kwiek, "Acousto-optic interaction of a gaussian laser beam with an ultrasonic wave of cylindrical symmetry," *Appl. Opt.*, vol. 46, pp. 5870–5876, Aug 2007.

[40] A. Grinenko, M. P. MacDonald, C. R. P. Courtney, P. D. Wilcox, C. E. M. Demore, S. Cochran, and B. W. Drinkwater, "Tunable beam shaping with a phased array acousto-optic modulator," *Opt. Express*, vol. 23, pp. 26–32, Jan 2015.

[41] M. C. Matteo G. Scopelliti, "Ultrasonic sculpting of virtual steerable optical waveguides in tissue," *Nature*, in press.

[42] Wikipedia contributors, "Numerical aperture — Wikipedia, the free encyclopedia." https://en.wikipedia.org/w/index.php?title=Numerical_aperture&oldid=862000307, 2018. [Online; accessed 3-October-2018].

[43] Amrita Laboratories, "Numerical aperture of optical fiber." http://vlab.amrita.edu/?sub=3&brch=189&sim=343&cnt=1, 2011. [Online; accessed 3-October-2018].

[44] Edmund Optics Inc., "Understanding microscopes and objectives." https://www.edmundoptics.com/resources/application-notes/microscopy/understanding-microscopes-and-objectives/, 2018. [Online; accessed 5-October-2018].

[45] J. Waters and T. Wittmann, *Quantitative Imaging in Cell Biology*. Methods in Cell Biology, Elsevier Science, 2014.

[46] Andor, "Rolling and global shutter." https://www.oxinst.com/learning/view/article/rolling-and-global-shutter, 2006. [Online; accessed 7-October-2018].

[47] Z. V. Guo, A. C. Hart, and S. Ramanathan, "Optical interrogation of neural circuits

in caenorhabditis elegans," *Nature methods*, vol. 6, no. 12, p. 891, 2009.

[48] F. B. Shipley, C. M. Clark, M. J. Alkema, and A. M. Leifer, "Simultaneous optogenetic manipulation and calcium imaging in freely moving c. elegans," *Frontiers in neural circuits*, vol. 8, p. 28, 2014.

[49] J. P. Nguyen, F. B. Shipley, A. N. Linder, G. S. Plummer, M. Liu, S. U. Setru, J. W. Shaevitz, and A. M. Leifer, "Whole-brain calcium imaging with cellular resolution in freely behaving caenorhabditis elegans," *Proceedings of the National Academy of Sciences*, vol. 113, no. 8, pp. E1074–E1081, 2016.

[50] J. F. Pasternak and T. A. Woolsey, "The number, size and spatial distribution of neurons in lamina iv of the mouse smi neocortex," *Journal of Comparative Neurology*, vol. 160, no. 3, pp. 291–306, 1975.

[51] William R. Schafer, "Neurophysiological methods in c. elegans: an introduction." `http://www.wormbook.org/chapters/www_intromethodsneurophys/intromethodsneurophys.html`. [Online; accessed 7-October-2018].

[52] B. A. Martinez, K. A. Caldwell, and G. A. Caldwell, "C. elegans as a model system to accelerate discovery for parkinson disease," *Current opinion in genetics & development*, vol. 44, pp. 102–109, 2017.

[53] R. Lints and Hall, "Male neuronal support cells, overview," 2009. [Online; accessed 10-October-2018].

[54] C. Fang-Yen, M. J. Alkema, and A. D. Samuel, "Illuminating neural circuits and behaviour in caenorhabditis elegans with optogenetics," *Phil. Trans. R. Soc. B*, vol. 370, no. 1677, p. 20140212, 2015.

[55] Simon Fraser University, "C. elegans nervous system." `http://www.sfu.ca/biology/faculty/hutter/hutterlab/research/Ce_nervous_system.html`, 2008. [Online; accessed 10-October-2018].

[56] W. Zhou, J. Wang, K. Wang, B. Huang, L. Niu, F. Li, F. Cai, Y. Chen, X. Liu, X. Zhang, *et al.*, "Ultrasound neuro-modulation chip: activation of sensory neurons in caenorhabditis elegans by surface acoustic waves," *Lab on a Chip*, vol. 17, no. 10, pp. 1725–1731, 2017.

[57] J. Larsch, D. Ventimiglia, C. I. Bargmann, and D. R. Albrecht, "High-throughput imaging of neuronal activity in caenorhabditis elegans," *Proceedings of the National Academy of Sciences*, p. 201318325, 2013.

[58] A. Ward, J. Liu, Z. Feng, and X. S. Xu, "Light-sensitive neurons and channels mediate phototaxis in c. elegans," *Nature neuroscience*, vol. 11, no. 8, p. 916, 2008.

[59] Kathryn Hedges, "Using improved 3% agarose pads with the paralytic levamisole for fluorescence microscopy of c. elegans." `http://wbg.wormbook.org/`, 2009. [Online; accessed 10-October-2018].

[60] M. B. Goodman, T. H. Lindsay, S. R. Lockery, and J. E. Richmond, "Electrophysiological methods for caenorhabditis elegans neurobiology," in *Methods in cell biology*, vol. 107, pp. 409–436, Elsevier, 2012.

[61] E. Kim, L. Sun, C. V. Gabel, and C. Fang-Yen, "Long-term imaging of caenorhabditis elegans using nanoparticle-mediated immobilization," *PloS one*, vol. 8, no. 1, p. e53419, 2013.

[62] S.-M. A. and L. H., "Microfluidics as a tool for c. elegans research." `http://www.`

wormbook.org/chapters/www_microfluidics/microfluidics.html, 2013. [Online; accessed 10-October-2018].

[63] Z.-J. Chen, G. T. Gillies, W. C. Broaddus, S. S. Prabhu, H. Fillmore, R. M. Mitchell, F. D. Corwin, and P. P. Fatouros, "A realistic brain tissue phantom for intraparenchymal infusion studies," *Journal of neurosurgery*, vol. 101, no. 2, pp. 314–322, 2004.

[64] R. Pomfret, G. Miranpuri, and K. Sillay, "The substitute brain and the potential of the gel model," *Annals of neurosciences*, vol. 20, no. 3, p. 118, 2013.